Journal of Materials Engineering and Performance

ASM INTERNATIONAL

The Effect of Jet Flow Impingement on the Corrosion Products formed on a Pipeline Steel in Naturally Aerated Sour Brine

Journal:	*Journal of Materials Engineering and Performance*
Manuscript ID	JMEP-18-03-15210.R2
Manuscript Type:	Technical Paper
Date Submitted by the Author:	31-Oct-2018
Complete List of Authors:	Domínguez-Aguilar, Marco; Instituto Mexicano del Petroleo, Produccion de Hidrocarburos y Control de la Corrosion Díaz-Cruz, Manuela; Instituto Politecnico Nacional, ESIQIE Cervantes-Tobon, Arturo; Instituto Politécnico Nacional , ESIQIE Castro-Domínguez, Bernardo; University of Bath, Chemical engineering
Keywords:	Corrosion and Wear, Microscopy, Electron, Modeling and Simulation, Steel, X-ray

The Effect of Jet Flow Impingement on the Corrosion Products formed on a Pipeline Steel in Naturally Aerated Sour Brine

M.A. Domínguez-Aguilar, [a,1] *M. Díaz-Cruz,* [b] *A. Cervantes-Tobón,* [b] *B. Castro-Domínguez* [c]

[a]*Instituto Mexicano del Petróleo, Dirección de Investigación, Eje Central Lázaro Cárdenas No. 152, Col. San Bartolo Atepehuacán, México D.F. 07730, México*

[b]*Instituto Politécnico Nacional, ESIQIE, Departamento de Metalurgia y Materiales, Av. Instituto Politécnico Nacional S/N, Col. Lindavista, México D.F. 07300, México*

[c]*University of Bath, Chemical engineering department, Claverton down, Bath BA2 7AY, England, United Kingdom*

Abstract

Corrosion was generated by the action of a jet impingement flow of sour brine on pipeline steel samples of X70. Flow assisted corrosion affected nature, number and peak intensity of the chemical species formed as corrosion products. Iron sulfides predominated in static and low flow rate conditions (1.1 m/s), whereas at 2.4 m/s iron oxides were mainly formed, which led to higher corrosion rates and suggested that oxides are less protective than sulfides. On inhibition, imidazoline seems to mitigate oxide formation and support sulfide formation balancing both species on steel surface. Ferrite phase in laminar pearlite was preferentially dissolved with/without inhibitor and mackinawite (FeS_2) was formed at every flow rate, angle with and without inhibitor. Theoretical stresses determined by computational flow dynamics for corrosion product removal showed a fair approximation to those proposed in the literature.

Keywords: Flow assisted corrosion (FAC); computational fluid dynamics (CFD), corrosion inhibitor (CI); corrosion products; experimental techniques

1. Introduction

[1] Corresponding author: Marco A. Domínguez-Aguilar (Tel: +5255-9175-8183, Fax: +5255-9175-7178, email: (madoming@imp.mx).

Carbon steel in acidic sour brine (pH 1-5) leads to aqueous corrosion by sulfide formation, in which corrosion process depends on iron oxidation, $Fe \rightleftarrows Fe + 2e^-$, and hydrogen evolution $2H^+ + 2e^- \rightleftarrows H_2$ after the dissociation of H_2S in liquid water, $H_2S \rightleftarrows H + HS^-$. This way overall electrochemical corrosion reaction can be described as:

$$Fe^{2+} + H_2S + 2H^+ + 2e^- \rightleftarrows FeS + 2H_2$$

The corrosion products formed on steel can be protective or porous depending on microstructure, composition, pH, temperature and time. The polymorphism and semi-conductive properties of sulfides make corrosion mechanism extremely complex to understand. Most chemical species are unstable and detrimental as the breakdown of the protective layers of iron sulfide permits that general and localized corrosion occur [1]. However, the nature of corrosion products formed might elucidate inherent mechanism and metal dissolution rates. The layers of corrosion products can be broken by the impact of flow viscous energy, which is created by the flow turbulence in the form of eddies and bubbles [2].

Flow assisted corrosion (FAC) is a common problem in equipment and pipeline systems pertaining to energy industry as flow dynamics contribute to a wall thickness reduction, cracking and failure by the continuous removal of corrosion products. Many studies of FAC involve a sudden change in flow direction as mass transfer is proportional to corrosion rate and dependent on flow geometry [3]. Impinging jet focuses flow against a surface to generate a high mass transfer so it is an attractive tool to study FAC [4]. Diverse studies have been performed to assess the effect of FAC on piping steels. Some authors have focused on the electrochemical characterization of carbonate corrosion scale as a function of impact angle, flow rate and shear stress to assess wall thinning [5]. Likewise, the effect of H_2S on the formation and growth of corrosion layers as a function of pH, chlorides and sulfides concentrations under different hydrodynamic conditions has been largely study to assess general corrosion and prevent localized corrosion [6]. Nesic and his group [7] have studied corrosion products to elucidate information of the background mechanism in H_2S/CO_2 in static/dynamic in completely anaerobic conditions. Film formation sequence and the superposition of corrosion layer products is a topic of importance [8]. Fracture mechanics as a tool to measure threshold stress and cracking for corrosion product removal and its correlation to FAC has been object of research

[9]. Another factor of relevance is the use of corrosion inhibitors (CI) as they provide a cost effective prevention method to control internal corrosion by forming a compact barrier between metallic surface/layers of corrosion products and electrolyte [10]. Stress level and corrosion rate determinations can provide an idea of wall reduction that combined with corrosion inhibitors might be successful in mitigating FAC. However, the effect of environment on the nature of corrosion products and how these chemical species affect corrosion rate of carbon steel in laminar and turbulent regimes is not fully understood. Studying the chemical species that conform the corrosion products, along with its morphology and structure, might provide the basis to understand FAC.

This work studies the effect of flow regime and contact angle on the nature of the corrosion products formed on carbon steel with and without the addition of corrosion inhibitor (CI) in naturally aerated sour brine. The composition of corrosion products and those formed on inhibitor films were determined by X-ray diffraction and scanning electron microscopy to gain a better understanding of how their features and morphology affected corrosion rate of carbon steel. Computational fluid dynamics (CFD) and theoretical calculations proposed in literature provided an approximate of stresses levels applied on the corrosion products formed on steel surface.

2. Experimental details

2.1 Materials and methods

Pipeline steel X70 was cut and machined into working electrodes of 0.5 cm^2 and 2 cm^2. Specimens were wet abraded with emery paper to 600 grits, mounted in resin and welded to an electric wire for connection. The jet impingement (JI) chamber consisted of a rectangular box made of acrylic with a volume capacity of 14 liters. It was provided with several drain pipes for fluid recovery and disposal. The JI chamber was manufactured with inlet/outlet connections as well as a movable plate, where metallic coupons are placed at the testing angles of 30 °, 60 ° and 90 °. A schematic diagram of the experiment set up is shown in Fig. 1.

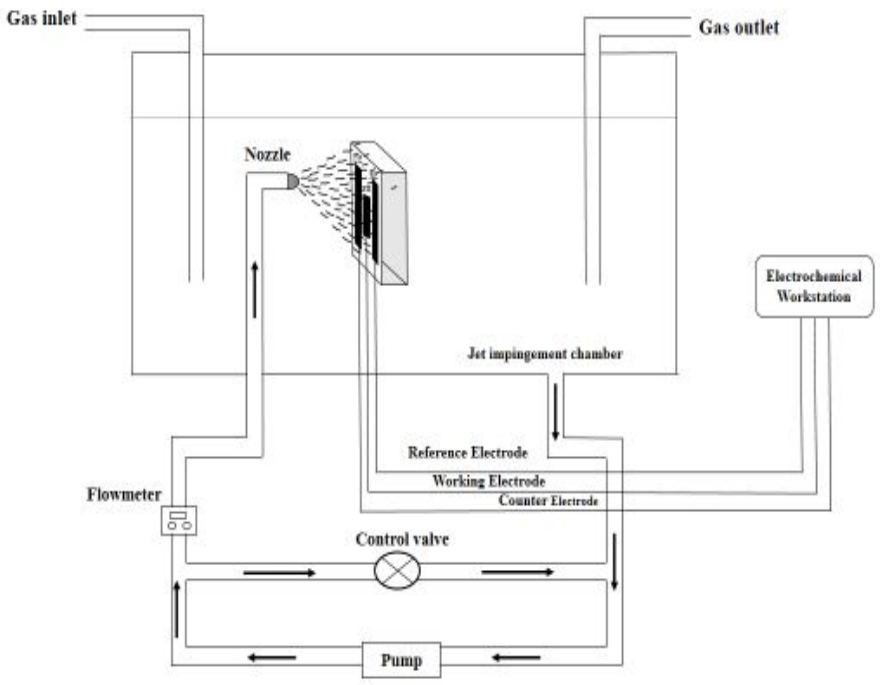

Fig. 1 Schematic diagram of the experimental setup to test flow assisted corrosion (FAC).

2.2. Corrosion rate measurements

Linear polarization resistance (LPR) measurements were performed in a standard electrochemical cell consisting of a working electrode (WE) of steel X70, a counter electrode (CE) of the same steel though with larger area and a reference electrode (RE) manufactured in SS316L. Experimental tests were controlled by the power suit software in a potentiostat-galvanostat PAR 2263A. The polarization scans were carried out on steel immersed in the testing electrolyte at ± 10 mV vs. the open circuit potential (OCP) at a rate of 0.166 mV/s inside the JI chamber. Corrosion rates were determined from polarization resistance measurements according to Stearn-Geary´s equation by means the R_p (ohm-cm^2) provided as a function of flow rate (1.1 m/s, 2.4 m/s) and testing time (1-8 hours), Procedure consisted in calculating the current density J_{corr} and corrosion rate as follows:

$$J_{corr} = \frac{B}{R_p} = \frac{\beta_a \text{ x } \beta_c}{2.3 \text{ x } R_p \text{ x } (\beta_a \text{ x } \beta_c)}$$

$$CR = \frac{0.00327 \text{ x } J_{corr}\,(\mu A/cm^2) \text{ x } EW}{\rho\ (g/cm^3)}$$

where β_a and β_c are the anodic and cathodic Tafel constants; 0.00327 is a constant used for conversion [11], EW is the equivalent weight of corroded iron (27.8 g/g mol) and ρ is the steel density (7.8 g/cm^3). In this study B is assumed to be 0.026 V; this data was taken from measurements performed at pH 4 [12] and whose slopes range within 60-120 mV/decade. The system under study stabilized itself at a roughly OCP within - 0.68 mV to - 0.73 mV in about 1 hour. Three tests were performed every hour to ensure reliability. Oleic imidazoline was added as CI once every 8 hours at a constant dosage of 200 ppm.

2.3 Computational Fluid Dynamics

2.3.1 Mesh design

The model to simulate the JI chamber was design in Solidworks [13] in order to conform a mesh of nodes and elements in agreement with the testing system (Fig. 2). This model has become largely useful as it permits to generate the process under study in real and simulated conditions. However, there should be selected suitable geometric and boundary conditions, mathematical models and numerical methods to generate reliable results. CFD determinations are commonly carried out by Ansys-Fluent, in which hydrodynamics parameters besides the thermodynamic properties of fluid are required to determine surface behavior under impact.

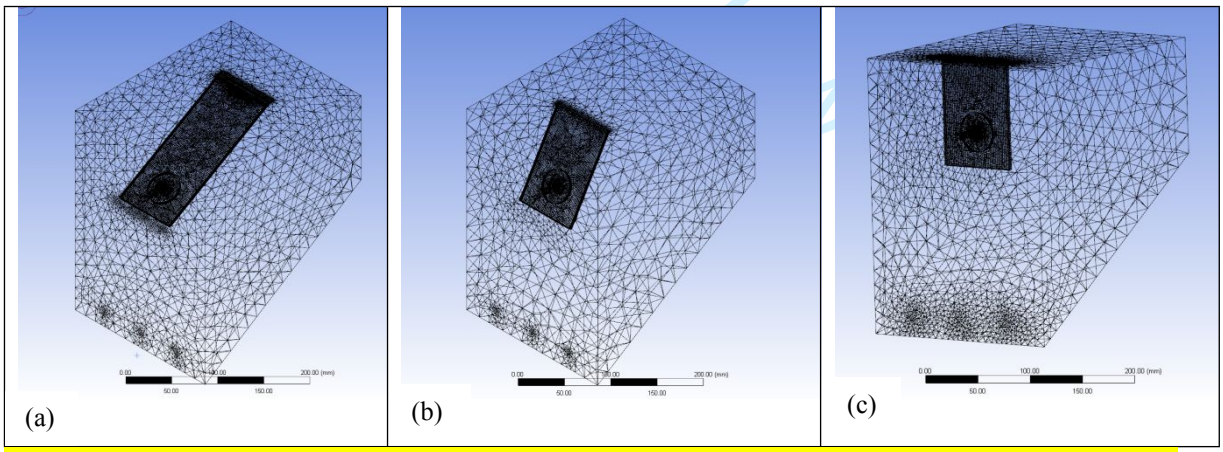

Fig. 2 Scheme of the network generated for the JI chamber showing the plate for the impact angles of (a) 30 °C, (b) 60 °C and (c) 90 °C.

The geometry model (Fig. 2) was imported to Ansys-fluent 14.5 for parameter calculations [14]. It consisted in a discretization of a series of triangular prisms that conformed the mesh for the JI chamber along with the plate located at the experimental impact angles. The mathematic model consisted in a series of partial differential equations transformed into algebraic equations by means of the convergence theorem, which quantitatively represents the process acting on each node to provide an integral solution for the parameters to be evaluated. The mesh generated for CFD calculations were composed of the following elements:

Angle	Nodes	Elements
30 °	110,003	337,654
60 °	56,953	200,448
90 °	83,792	399,936

2.3.2 Computational Fluid Dynamics (CFD)

CFD is a numerical technique that requires the solution of the Navier-Stokes equations to find the flow field for the system under study. The flow behavior is governed by the solution to Newtonian incompressible fluid equations for mass, momentum, energy and other species transported in the domain. The conservation of mass (continuity equation) can be written as:

$$\frac{\partial \rho}{\partial t} + \frac{\partial}{\partial x_j}\left(\rho u_j\right) = 0 \tag{1}$$

$$\frac{\partial}{\partial t}\left(\rho u_i\right) + \frac{\partial}{\partial x_j}\left(\rho u_i u_j\right) = -\frac{\partial \mathrm{P}}{\partial x_i} + \frac{\partial}{\partial x_j}\left[\mu_{eff}\left(\frac{\partial u_i}{\partial x_j} + \frac{\partial u_j}{\partial x_i}\right)\right] + \rho g \tag{2}$$

Turbulence effects were resolved by the mathematical model proposed by Jones and Launder [15, 16] known as the κ-ε turbulent model, which is a semi-empiric approach based on transport equations for the turbulent kinetic energy (κ) and its dissipation rate (ε). Methodology assumed that flow is completely turbulent and molecular viscosity is negligible; turbulent kinetic energy and its dissipation rate are described as follows:

$$\frac{\partial}{\partial t}(\rho k) + (\rho u_i k - \frac{\mu_{eff}}{\sigma_k}\frac{\partial k}{\partial x_i}) = G - \rho\varepsilon \quad (3)$$

$$\frac{\partial}{\partial t}(\rho\varepsilon) + \frac{\partial}{x_i}(\rho u_i \kappa - \frac{\mu_{eff}}{\sigma_\varepsilon}\frac{\partial k}{\partial x_i}) = \frac{\varepsilon}{\kappa}(C_1 G - C_2 \rho\varepsilon) \quad (4)$$

where:

$$G = \mu_t \frac{\partial \mu_i}{\partial x_i}\left(\frac{\partial \mu_i}{\partial x_i} + \frac{\partial \mu_j}{\partial x_j}\right) \quad (5)$$

where, ρ = density; *k* is the turbulent kinetic energy; ε = rate of dissipation of turbulent kinetic energy; u = velocity vector; u_i = i^{th} component of the velocity vector; ν = kinematic viscosity; μ = dynamic viscosity; σ_k = Prandtl number for the turbulent kinetic energy; σ_ε = Prandtl number for the dissipation rate; *G* = turbulent kinetic energy generated from the mean velocity gradients; C_1 = first experimental model constant for the dissipation rate; C_2 = second experimental model constant for the dissipation rate. The effective viscosity is the sum of the laminar and turbulent viscosities, $\mu_{eff} = \mu_l + \mu_t$. Other scalar and pressure quantities are described as, $\phi_{eff} = \phi_l + \phi_t$. The substitution of effective viscosity in equations (1) and (2) besides placing the mean velocity yields the ensemble-averaged momentum equations. They have the same general form of the instantaneous Reynolds-averaged Navier-Stokes equations with the velocities and other solution variables now as time-averaged values.

2.3.3 Boundary conditions

The fluid was assumed to be incompressible and the turbulence dissipation model κ-ε was used for flow analysis; κ refers to the turbulent kinetics energy and *ε* refers to its local rate of dissipation. Simulation was set as follows: CFD calculation finishes when error ≥ 1 x 10^{-3}. Experimental conditions for the immersed jet flow impingement device coincide with those proposed elsewhere [17, 18]. Inlet conditions: Electrolyte entered at a flow rate of 1.1 and 2.4 m/s, with a dynamic viscosity of 0.44×10^{-3} Pa/s and a density of 0.98×10^{3} kg/m^3. The test temperature was 30 ℃. Fluid was assumed to be incompressible with constant properties. κ-ε turbulent model was used to numerically solve partial equations. Turbulence intensity was set

at 10%. The turbulent kinetic energy, κ, was set at 1 J/kg and the turbulent dissipation, ε, was 1 W/kg for simulation. Outlet conditions: Electrolyte exited at atmospheric pressure (101.3 kPa).

2.3.4 Model validation

Model validation is the primary means to assess accuracy and reliability in computational simulations. The jet flow impingement experimental model has been the object of several studies in fluid mechanics for Newtonian fluids [19-21]. The shear stress induced by turbulence on corrosion products is the parameter to be evaluated. In laminar flow, the viscous energy loss within the turbulence boundary layer is defined by the normal velocity gradient at the wall as:

$$\tau = \mu_t \frac{\partial v}{\partial n} \tag{6}$$

In turbulent flow, the shear stress is derived from κ-ε model as:

$$\tau_{ij} = -\rho\overline{u_i' u_j'} = \mu_t\left(\frac{\partial U_i}{\partial x_j} + \frac{\partial U_j}{\partial x_i}\right) \tag{7}$$

The model validation for the jet flow impingement has been done previously by several authors, who considered the effect of the layer supposition of corrosion products formed on surface. D-J. Peng *et al*. [22] determined the wall shear stress in pipe by Fluent CFX based on the validated model of Ewing *et al.* [23]. Cai *et al.* [18] studied the electrochemical behavior of pipe steel at high pressure and high temperature under jet flow conditions, in which model validation was based on colleagues work by the CFD calculations of shear stresses [17]. Nesic *et al.* [24] validated an erosion corrosion model by comparing flow parameters in a scale model with a series of computational simulations. For the present study, the shear stresses were determined by the κ-ε model, which were compared with the results derived from the equations of Giralt-Trass [25, 26] and Efird [27].

3. Results and discussion

3.1. Steel composition and microstructure

The chemical composition of the pipeline steel X70 was determined by optical emission spectroscopy in a bow and spark spectrometer (BELEC). Composition of pipeline steel API X70 was as follows (wt. %): 0.24 C, 1.08 Mn, 0.284 Si, 0.019 P, 0.021 S, 0.156 Cr, 0.185 Cu, 0.088 Ni, iron balance. Microstructure of steel X70 (Fig. 3) consisted of a uniform distribution of ferrite (65.4%) and lamellar pearlite (34.6%) conformed in colonies and distributed in a matrix of ferrite of a normalized carbon steel with an average grain size of 10 units.

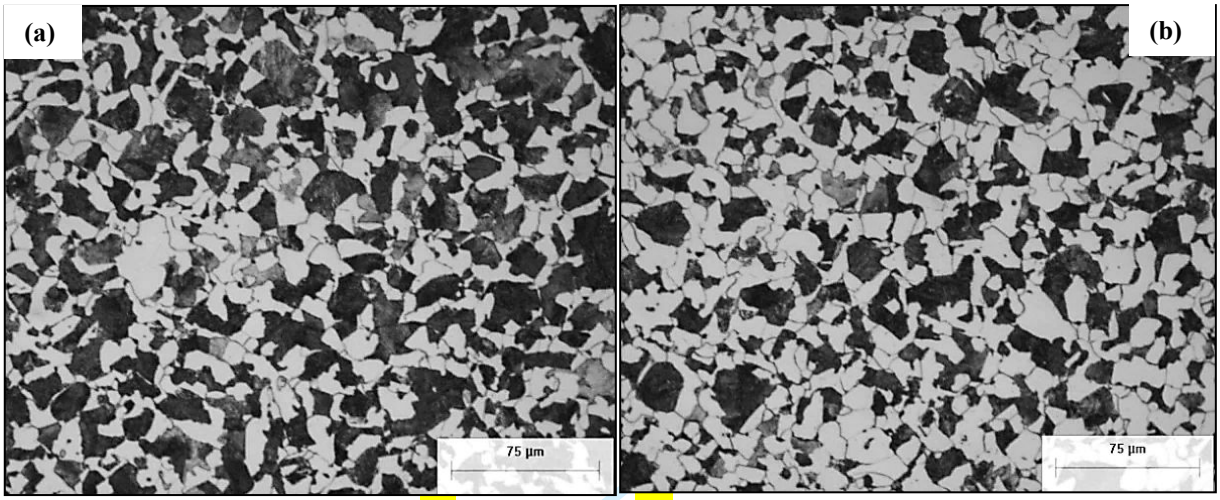

Fig. 3 Microstructure of internal (a) and external (b) sections of pipe steel X70 etched in 5% Nital, showing ferrite and pearlite in light and dark contrast, respectively (500X).

3.2 Physical model and jet flow impingement

Fig. 4 shows several images of the interior of JI chamber after the CFD simulation at a flow rate of 2.4 m/s for the different impact angles. The turbulence inside the JI chamber (Fig. 4a) appeared to be similar to the flow density (Fig. 4b) and flow distribution (Fig. 4c) generated. It is observed that both flow density and turbulence increased as the angle increased from 30 ° to 90 °, which can be ascribed to an increase in friction forces when tilting plate angle is raised as flow resistance is increased. Flow lines also described the presence and location of a stagnation region, in which flow rate is the highest in the system. In this case, it appears that an area of high sensitivity is directly located in front of the flow entrance for the impact angle of 90 °, which is critical in the normal plane position. Flow lines provided an example of reliability as the parameters behind these lines are useful in determining flow velocity and flow patterns.

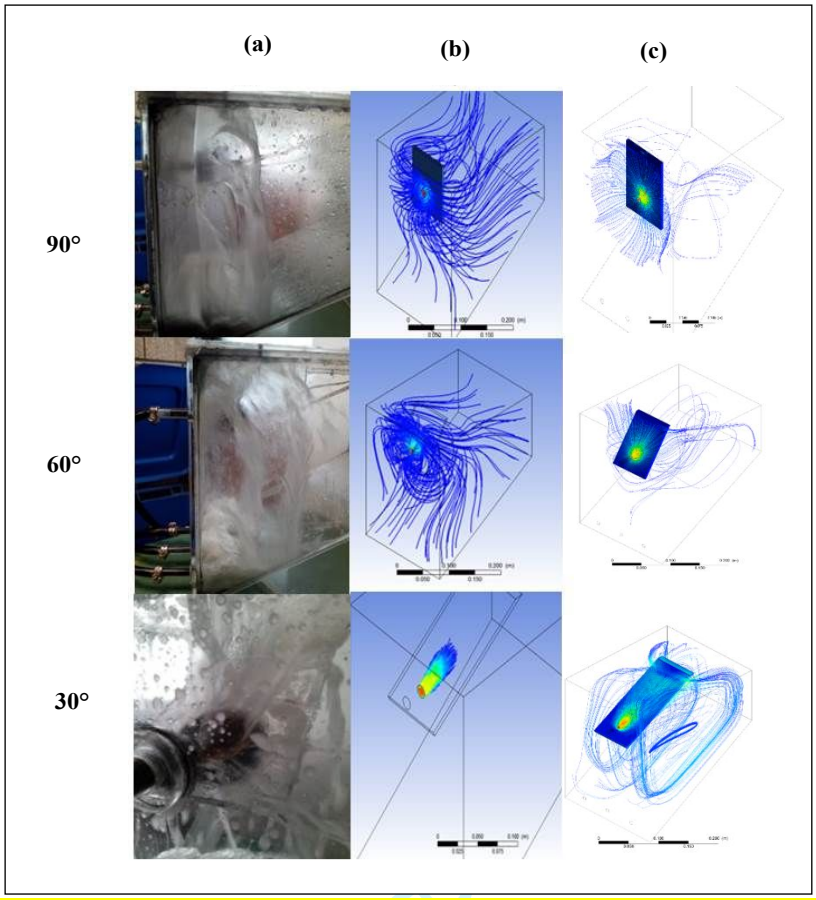

Fig. 4 CFD simulation in the JI chamber showing: (a) Inner flow turbulence produced by impinging on holding plates at the angles indicated; (b) flow density and (c) flow lines at 2.4 m/s.

3.3 Shear stress distribution

Fig. 5 shows the distribution of shear stress on the JI plate under the action of a flow rate of 1.1 m/s and 2.4 m/s for the angles of 30 °, 60 ° and 90 °. For 2.4 m/s at 30 ° and 60 °, shear stresses displayed an anti-symmetric distribution, which is homogenously maintained on the working electrode, where the highest stresses reached 15-20 N/m^2 (1.1 m/s) and 33-40 N/m^2 (2.4 m/s). At 90°, the shear stress is symmetrically distributed on the metallic coupon reaching a magnitude of about 8.6 N/m^2 (2.4 m/s). The shear stress increased as the mass flow rate was increased from 1.1 m/s to 2.4 m/s for the impact angles tested. Table 1 summarizes the highest shear stresses determined by CFD for both mass flow rates. It is worth noticing that shear stress decreased as

the impact angle is increased, i.e. stress changes from shear to normal as angle increased; these results are in agreement with those observed by Zhang *et al.* [28].

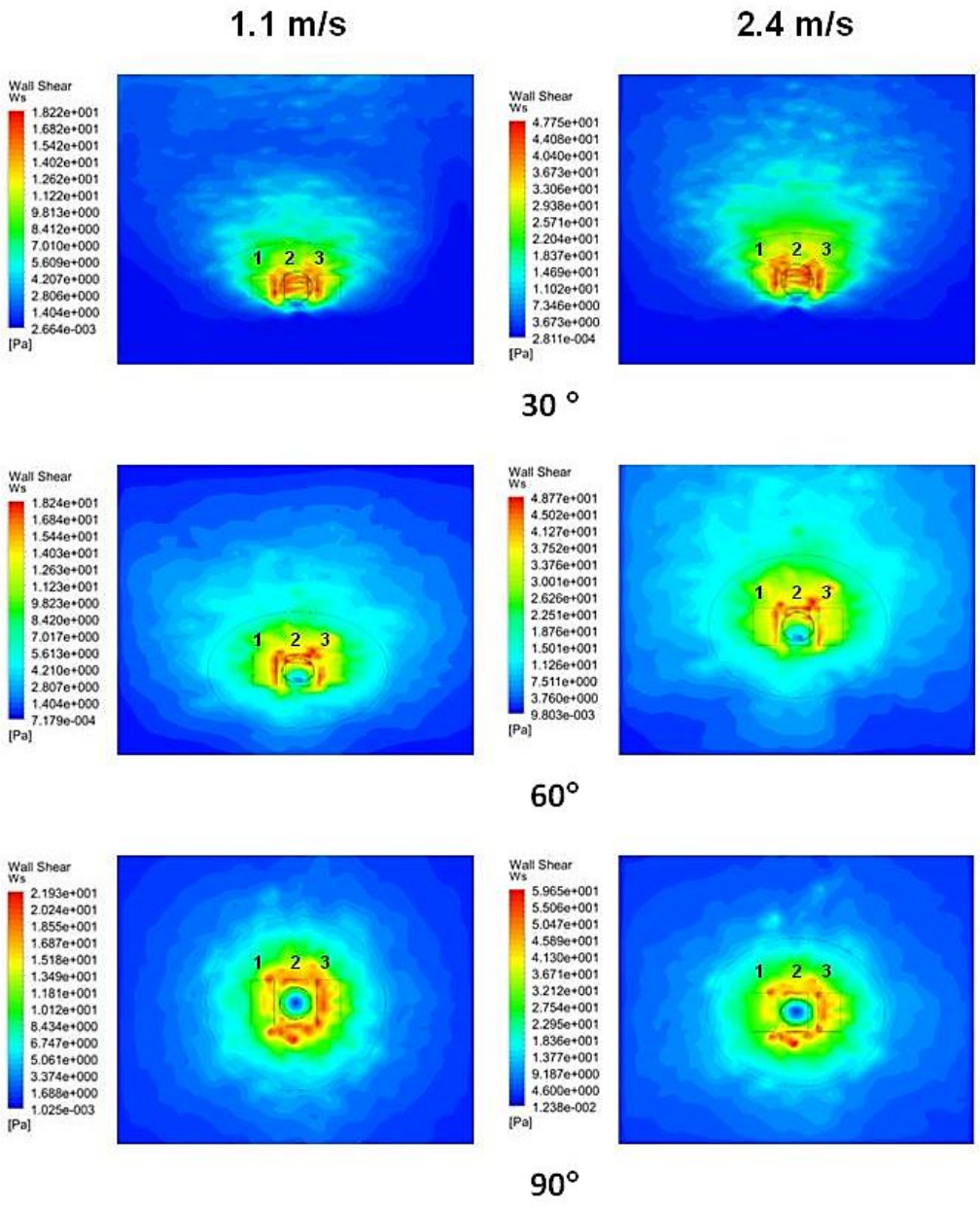

Fig. 5 Distribution of shear stress on steel coupons of X70 under the action of flow rate and impact angles.

For coupons in the positions 1 and 3 on sample edges, shear stress followed the same tendency i.e. it decreased when impact angle is increased. The change in impact angle generated deformed regions to one side (30 °, 60 °), and regions with central symmetry (90 °). The former showing an asymmetric behavior with the lowest shear stress on coupon 3 at 30 ° (12-33 N/m^2); an intermediate level of stress at 60 ° (17-41 N/m^2) and the highest shear stress at 90 ° (41-53 N/m^2) as coupon 3 is the location of the transition region for each of the angle positions.

3.4 Turbulence distribution

Fig. 6 shows the frontal view of the metallic coupon set on the jet plate at different impact angles, when flow rate is 2.4 m/s. At 30 °, a turbulence energy of 0.04 J/kg is generated, while at 60 ° increased to 0.08 J/kg and for 90 ° reached 0.043 J/kg. As mass flow rate is increased, shear stress on coupon at position 2 decreased and turbulence increased. In contrast, shear stress increased and turbulence decreased at positions 1 and 3; this behavior was practically the same at 1.1 m/s. At 30 ° and 60 °, the shear stresses and turbulence are asymmetrically distributed acting first in the lower part of the metallic coupons and moving upwards on the coupon surface. At 90 °, both parameters acted symmetrically on the coupon surface and this behavior was recorded for both mass flow rates (Table 1). It is observed that there exists a tendency in which turbulence energy increased as the impact angle was increased.

The shear stress is related to the fluid viscous energy acting on a wall consequently, this force is inside the fluid and interacts with the steel surface. This parameter has an important role in the removal of layers of corrosion products and on the inhibitor films formed on corrosion products that protect metallic surface. This force is applied on the working electrode on specific regions and can vary depending on fluid properties, mass flow rate, impingement angle, and sometimes layers of products/films can be removed continuously so corrosion rate is enhanced as new metal is exposed to the environment. Another parameter provided by CFD is the velocity vector for the hydrodynamic conditions on testing, the distribution of this parameter is shown in Fig. 7. The velocity vector decreased with the increase in the impingement angle from 30 ° and 90 ° for 1.1 m/s and 2.4 m/s, though the highest value occurred at 30 ° > 60 ° > 90° at the impact region (Table 1).

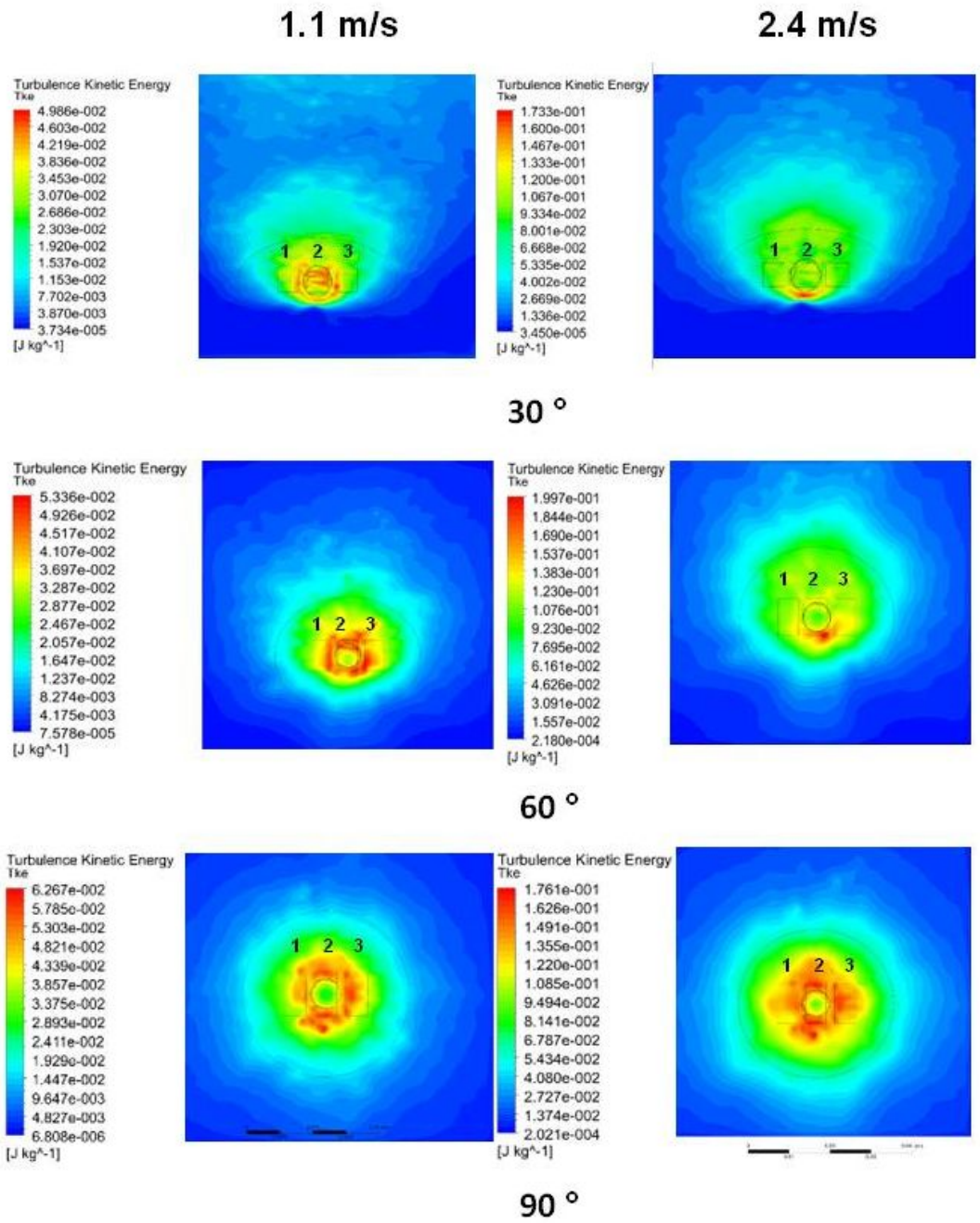

Fig. 6 Distribution of the kinetic energy of turbulence on steel coupons of X70 at the flow rate and impact angle indicated.

Another parameter provided by CFD is the velocity vector for the hydrodynamic conditions on testing, the distribution of this parameter is shown in Fig. 7. The velocity vector decreased with the increase in the impingement angle from 30 ° and 90 ° for 1.1 m/s and 2.4 m/s, though the highest value occurred at 30 ° > 60 ° > 90° at the impact region. Table 1 summarizes the highest shear stresses determined by CFD for both mass flow rates. It is worth noticing that shear stress

decreased as the impact angle is increased, as the acting stress changes from shear to normal as angle increased; these results are in agreement with the former experimental flow rates.

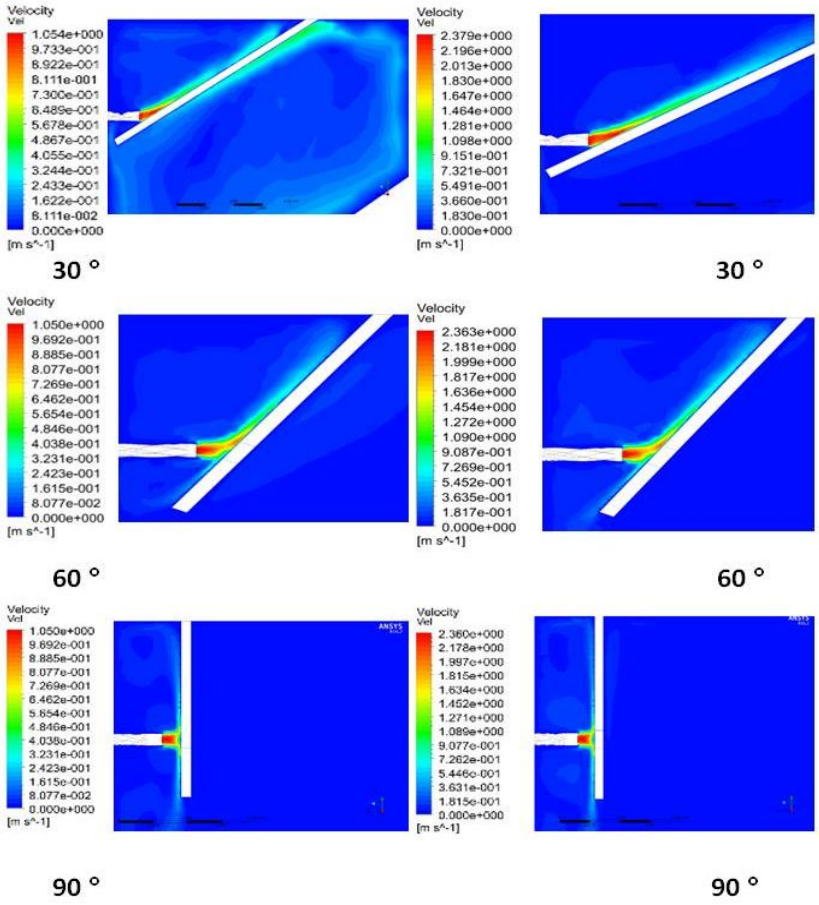

Fig. 7 Distribution of the velocity vector on the impingement steel coupons of X70 at the flow rate and impact angle indicated.

Table 1. Average highest values of shear stresses, turbulence energy and velocity for the metallic coupon at position 2

Impact angle	30 °	60 °	90 °
Average shear stress at 1.1 m/s, Pa / N/m^2	12.6	7.5	6.7
Average shear stress at 2.4 m/s, Pa / N/m^2	33.0	15.0	8.6
Turbulence energy (J/kg) at 1.1 m/s	0.04	0.08	0.043
Turbulence energy (J/kg) at 2.4 m/s	0.04	0.10	0.14
Velocity vector at 1.1 m/s	1.05	0.81	0.5
Velocity vector at 2.4 m/s	2.38	1.8	1.1

3.5 Corrosion rates determined by LPR

Fig. 8 shows the changes in corrosion rate as a function of immersion time after linear polarization resistance measurements for a mass flow rate of 1.1 and 2.4 m/s at 90 °, where the highest corrosion rates were recorded. Corrosion rate tended to decrease as testing time was increased as a result of film formation by corrosion products. Likewise, corrosion rates decreased in the presence of 200 ppm of imidazoline, which inhibits corrosion by film formation on steel surface.

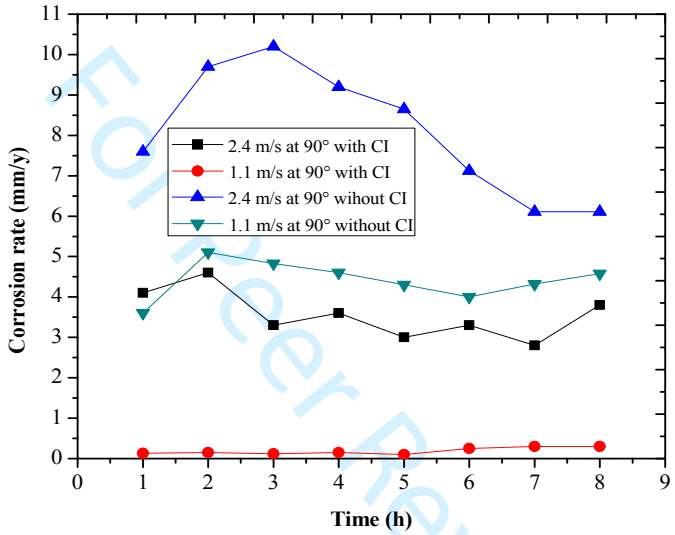

Fig. 8 Corrosion rate at a flow rate of 1.1 m/s and 2.4 m/s (a) without CI, and (b) with CI at an angle of impingement of 90 °

3.6 Relationship between normal/shear stress and corrosion rate

The normal stress generated at 90 ° can be determined by the normal pressure acting on the working electrode [29], P_s/A, which is described as:

$$P_s = \frac{1}{2}\rho U_0^2 \quad (8)$$

where ρ = density (kg/m^3); U_0 = flow velocity at leaving point (m/s); and A = cross sectional area (m^2) . The stagnation region (Fig. 9d region A) located exactly below the flow is the location where normal stress is maximum and shear stress is minimum. The normal stress at the stagnation zone (Fig. 9c) apparently resulted to be in the range of that obtained after CFD simulation, which may account for the higher corrosion rate experimented at 90 °. This finding

coincides with the highest rate of erosion corrosion that occurred in the stagnation region immediately beneath the jet, where particles impacted the surface at angles near 90 ° (Fig. 9a) [30, 31]. Further calculations of the shear stress (Fig. 9c) by CFD and some of those cited in the literature are compared at 1.1 and 2.4 m/s (Table 2).

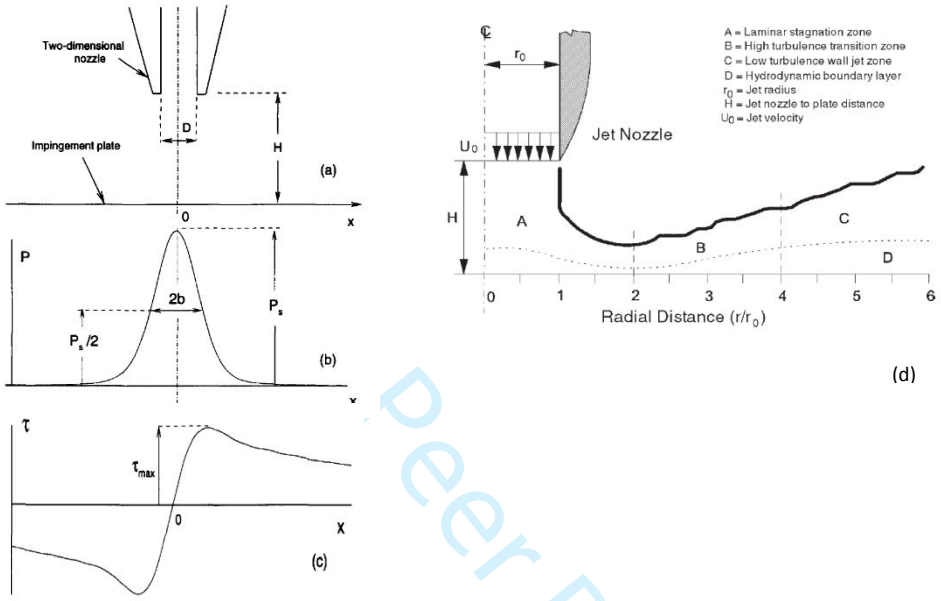

Fig. 9 (a) Jet nozzle and impingement plate (b) Highest normal stress and (c) Highest shear stress under the action of jet impingement on metallic surface in submerged conditions [32], and (d) a schematic diagram of the JI system along with flow patterns after impingement [33]

Giralt and Trass [25, 26] originally proposed a formula to calculate the shear stress under turbulence in the wall jet region, in which r/r_0 is within 2 to 4 units (Fig. 9d, region d). The equation for the wall shear stress [34] is described as:

$$\tau_w = 0.179\ \rho\ U_0^2 R_e^{-0.182} (r/r_0)^{-2} \quad (9)$$

where the jet Reynolds number, $R_e = 2\ r_0\ U_0\ (1/\nu)$ with $\nu = \mu/\rho$, is defined differently from conventional calculations, where τ_w = wall shear stress (N/m^2); ρ = density (kg/m^3) of sour brine (1025 kg/m^3); U_0 = flow velocity at leaving point (1.1/2.4 m/s); r = is the radial distance from the jet center line (0.01 m); r_0 = jet nozzle radius (0.005 mm); Re = Reynold´s number and ν = kinematic viscosity of testing fluid (1.046 m^2/s). Calculations of shear stress by CFD and authors are summarized in Table 2. K.D. Efird proposed a general equation to determine corrosion rate generated in carbon steel materials exposed to brine [27, 35], i.e. an aqueous solution containing sodium chloride and carbon dioxide/hydrogen sulfide under a turbulence regime by means of

calculating the shear stress evolved on the contact surface by means of $R_{corr} = a\,\tau_w^{\,b}$, where R_{corr} = corrosion rate of carbon steel [mm/y]; τ_w = shear stress on contact surface [Pa = N/m^2]; a and b = constants that correlate environment and chemistry. For a jet impingement device: a = 6.8 mm/y (299 mpy) and b = 0.095 for $r/r_0 = 3$ so the shear stress is defined as $\text{Log } R_{corr} = \text{Log } a + b \text{ Log } \tau_{wcorr}$. This correlation can be described by a linear equation $y = b + m\,x$. When corrosion rate values previously determined under jet impingement tests are applied, the shear stress determined is compared to that provided by CFD simulation. In this case, when corrosion rate increased shear stress also increased and consequently this implies that corrosion products might be removed, depending on the stress level generated in the flowing system. In Fig. 10, it is observed the correlation between corrosion rate and shear stress based on Efird´s equation [35] for the experimental data obtained in this work. A logarithmic dependence is shown for these parameters after being tested under laminar and turbulent flow patterns, produced at 1.1 m/s and 2.4 m/s, respectively. The highest shear stress derived in the highest corrosion rates though in the experimental work did not completely correlate. It is observed that an increase in flow rate involved an increase in shear stress, as some minor changes in constants are required to adjust to flow pattern and consequently to the r/r_0 ratio of the system [36, 37]. Corrosion rate at 1.1 m/s reached only 5 mm/y after eight hours, whereas at 2.4 m/s is approximately 11 mm/y after 4 hours. The lack of coincidence with Efird´s equation at 1.1 m/s is probably ascribed to the presence of a laminar flow pattern.

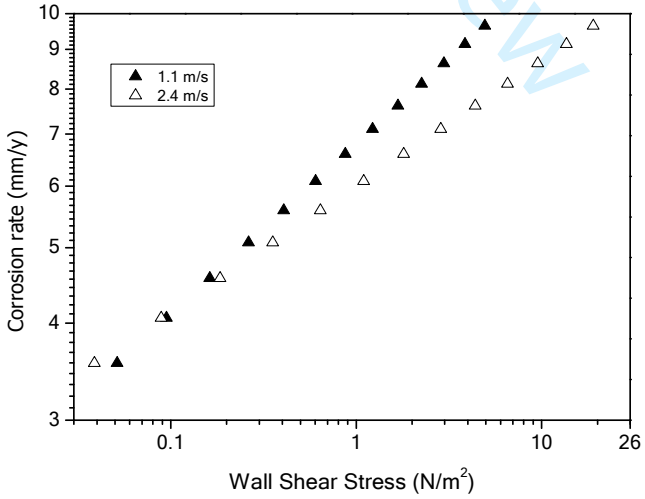

Fig. 10 Wall shear stress determined according to Efird´s equation from the experimental data of corrosion rate obtained in the JI chamber at 90 °.

The attraction of jet impingement testing is that the corrosion patterns and weight loss obtained on test specimens appear to be typical of those observed in practice. The jet impingement system produces the required local turbulence intensity and shear stress found in real conditions [38]. Table 2 summarizes the theoretical shear stresses calculated by means of CFD and by those correlations provided by authors studying FAC by jet impingement. The average shear stresses calculated by CFD (8.7 Pa, 19 Pa) is in the range of those calculated theoretically, though approximation could be improved by modifying flow equation to take into consideration the effect of impact angle. In the case of the normal stresses, when compared to the shear stresses yielded at 90 °, those of Phares *et al.* [33] exceeded by far those calculated by CFD and in consequence corrosion rate tended to be higher at 90,° even higher than those generated by the shear stresses at 30 ° and 60 °. At the latter angles, shear stress predominated over normal stress, that is to say the former ones were higher than their corresponding normal stresses. Likewise, shear stress calculation to remove corrosion products is roughly in the range of ~100-200 Pa, while it might be required a force of ~1000-2000 Pa to remove the film formed by chemical treatment in multiphasic flow. However, flow regime, composition, CI concentration and treatment became critical parameters to improve approach to real conditions and stresses [39-41].

Table 2. Average stresses for monophasic flow at 1.1-2.4 m/s

	Shear stress by CFD Pa / N/m²			**Theoretical shear stress Pa / N/m²**		**Normal stress Pa / N/m²**
Impact angle	30 °	60 °	90 °	Giralt-Trass [25, 26]	Effird (90°) [27]	Phares [32]
Average shear stress at 1.1 m/s	12	7.5	6.7	5.3	6.2	620
Average shear stress at 2.4 m/s	33	15	8.6	21.7	10.1	2880

3.7 SEM after jet impingement tests

Fig. 11 shows the SEM images for the coupon surfaces after the corrosion tests at 1.1 m/s; at 25X magnification, a general attack on surfaces is observed along with remains of corrosion products and salt grains. At 300X, some localized corrosion is observed at 90 °, whereas at a

magnification of 1500X, the dissolution of ferrite phase is observed (white contrast). The microstructure of carbon steel, in absence of inhibitor, consisted of ferrite and perlite. The presence of micro-galvanic cells between cementite and ferrite within pearlite resulted in a selective attack at and around pearlite bands. A similar effect has been reported with the continuous dissolution of ferrite in pearlite region, in which cementite between two lamellas may be undermined and stripped off the pearlite region. This leads to the aspect of grooves on the metal surface [42, 43], which coincides with the images shown at 1500X in Figs. 11c and 12c. Another surface feature is porosity, this is evident at 1.1 m/s (25X) and it seems to increase as the impingement angle is increased. Likewise, ferrite dissolution was intensified as the impingement angle was increased (Figs. 11a-c). In the presence of inhibitor steel surface conformed a heterogeneous protective film. Similarly, the samples tested at a flow rate of 2.4 m/s (Fig. 12) display an intensified corroded surface, in which is more evident the removal of metal from surfaces together with salt deposits. The samples with inhibitor show a film conformed of rounded particles forming a compact layer with morphology of rose bud. (Figs. 11d, 12d). At low flow rate (1.1 m/s), a more dense and adherent layer conforming a more protective layer is observed [8]. Precipitates of salt are observed as round particles of white bright contrast on both set of surfaces; these features are derived from the composition of the sour brine used as electrolyte. High flow rates are believed to accelerate general corrosion and might induce localized corrosion [44]. Likewise, when the flow rate increases the scour effect intensifies and washes the loose corrosion products increasing corrosion rate.

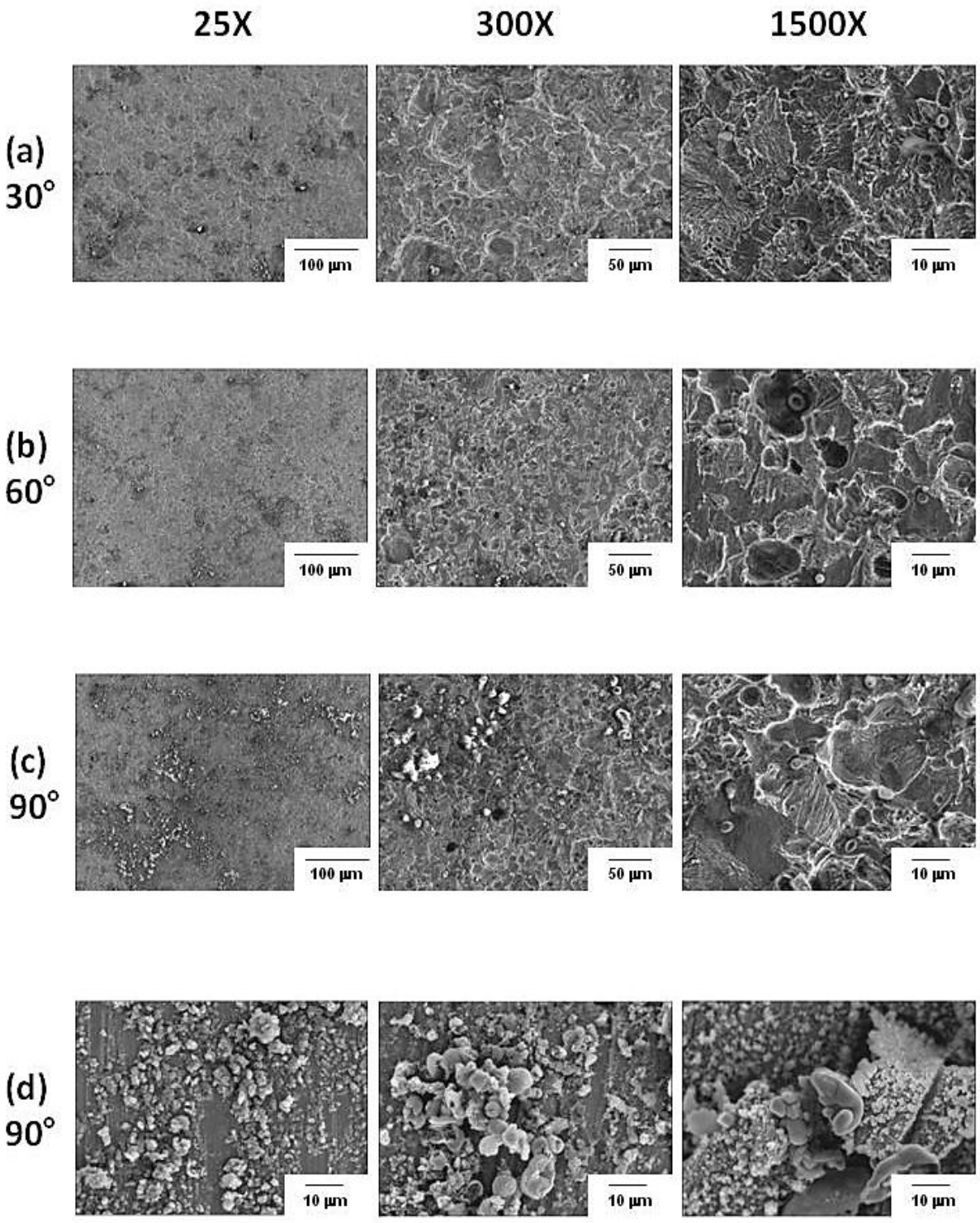

Fig. 11 SEM micrographs of X-70 in naturally aerated sour brine without inhibitor (a-c) and with inhibitor (d) after 8 h at l.1 m/s

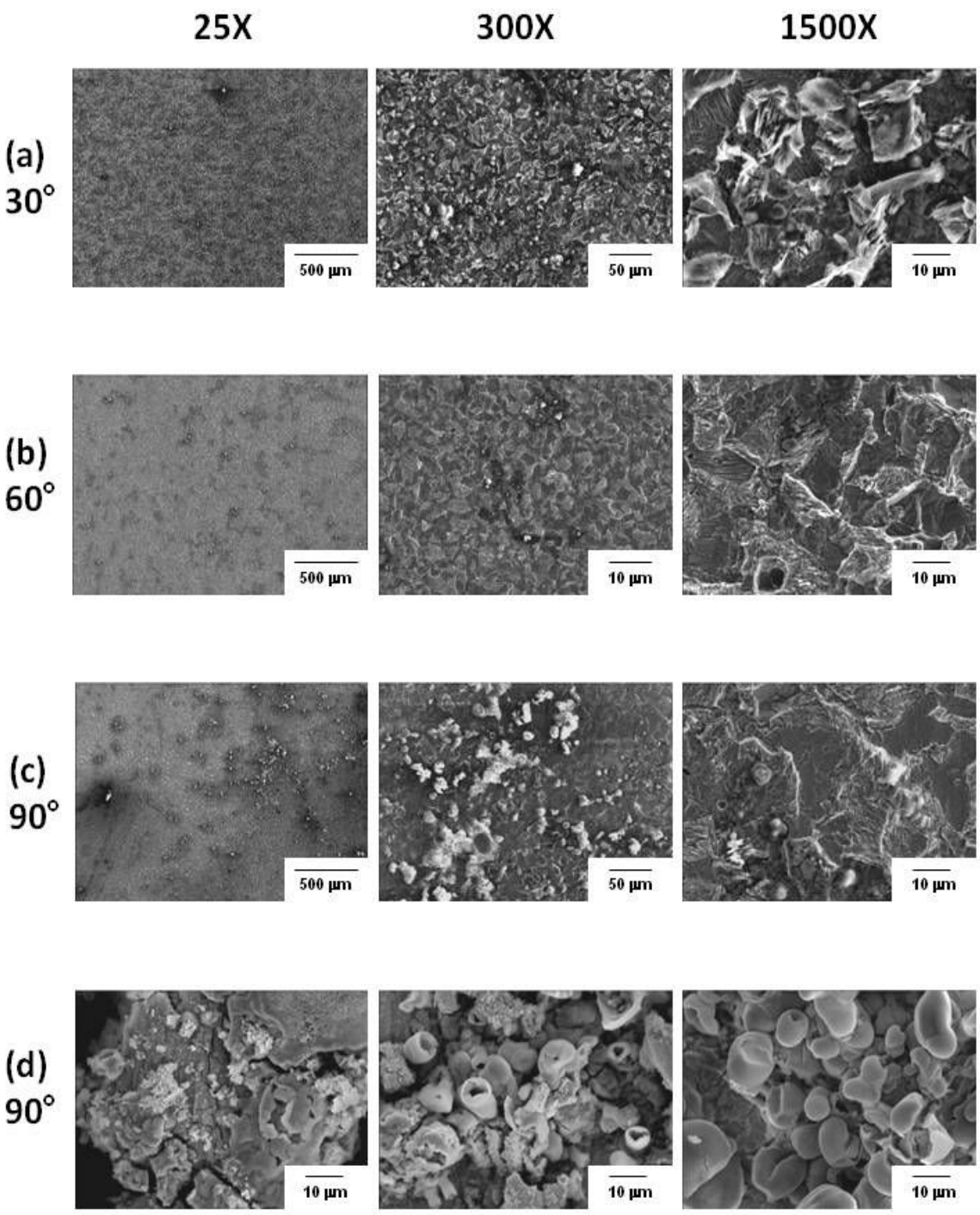

Fig. 12 SEM micrographs of X70 in naturally aerated sour brine without inhibitor (a-c) and with inhibitor (d) after 8 h at 2.4 m/s.

3.8 X-ray diffraction analyses (XRD)

The corrosion products of pipeline samples of steel X70 were analyzed by XRD after an immersion test of 24 hours performed in an environment of sour brine naturally aerated. Fig. 13 shows the diffraction pattern in static conditions, in which sulfides seems to predominate over oxides. The presence of mackinawite (FeS) as a base precursor on which others layers of corrosion products grew is quite evident as a basis line [8]. It appears that Fe_2O_3/Fe_3O_4 appeared to be derived from oxygen contamination as maghemite (Fe_2O_3) is the only oxide that is clearly shown (~2,000 a.u.). However, the layers of corrosion products seems to be conformed of rhombohedral hematite (Fe_2O_3), tetragonal hematite (Fe_2O_3), cubic maghemite (γ-Fe_2O_3), orthorhombic magnetite (Fe_3O_4), cubic magnetite (Fe_3O_4), orthorhombic marcasite (FeS_2) and cubic pyrite (FeS_2) with countings within 1000-1600 a.u. These corrosion products are equivalent to the iron sulfides reported by Y. Zheng *et al.* [45], who emphasized the importance of polymorphism of crystalline phases on the mechanical properties and corrosion resistance of products/films, except for the presence of marcasite (FeS_2). It is worth noticing that corrosion resistance of crystalline corrosion products is as follows: mackinawite < troilite < pyrrhotite < marcasite < pyrite [46].

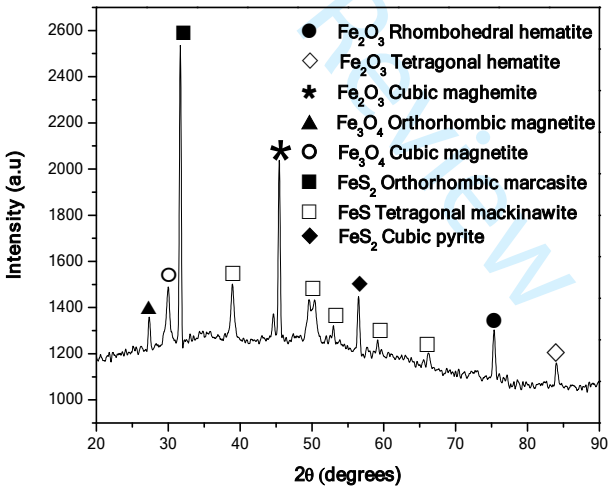

Fig. 13 XRD pattern of the corrosion products formed on steel in static condition after an immersion for 24 hours in naturally aerated sour brine.

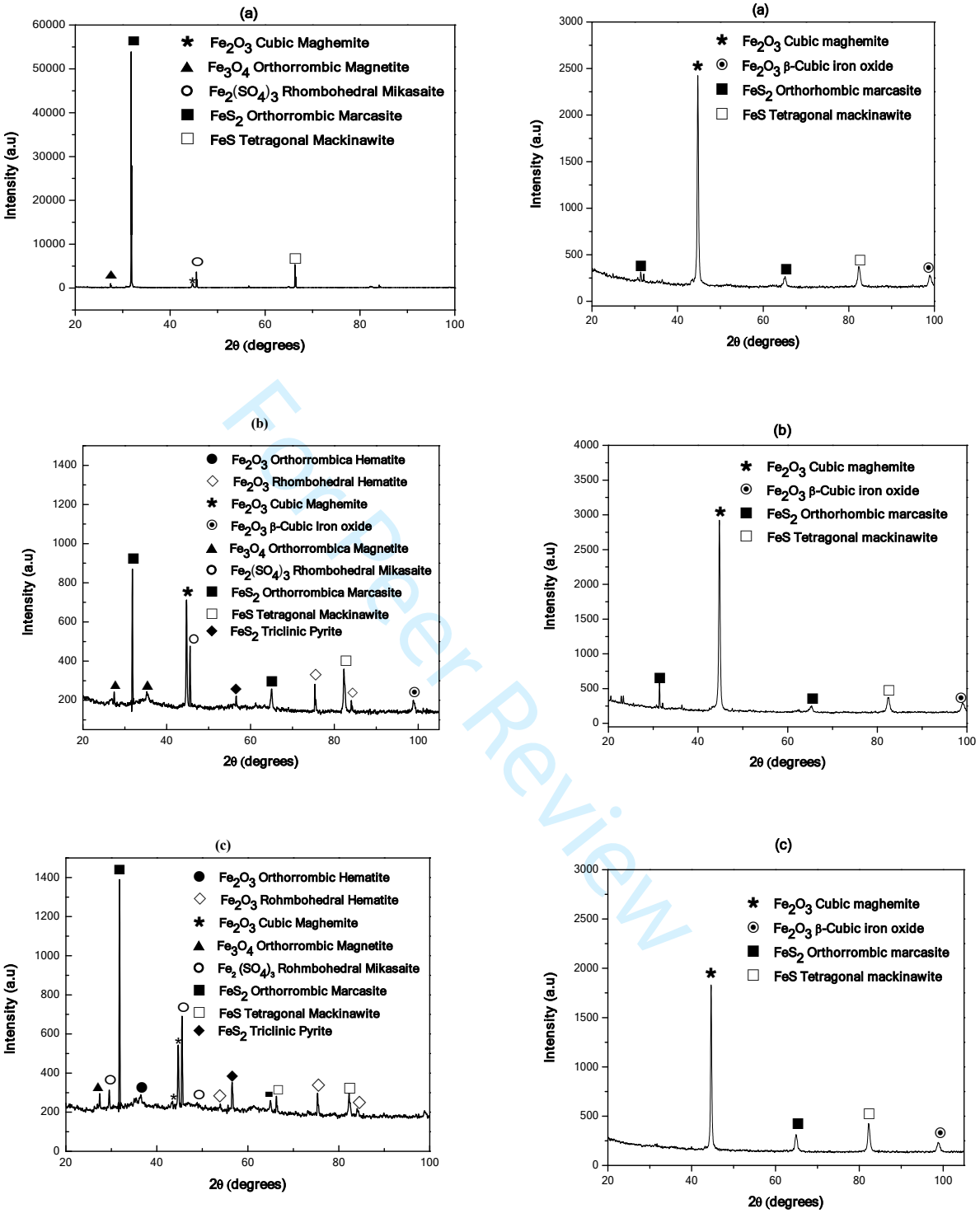

Fig. 14 XRD patterns of the corrosion products formed on steel surface in naturally aerated sour brine without CI (a) 30 °, (b) 60 ° and (c) 90 ° at 1.1 m/s (left) and 2.4 m/s (right).

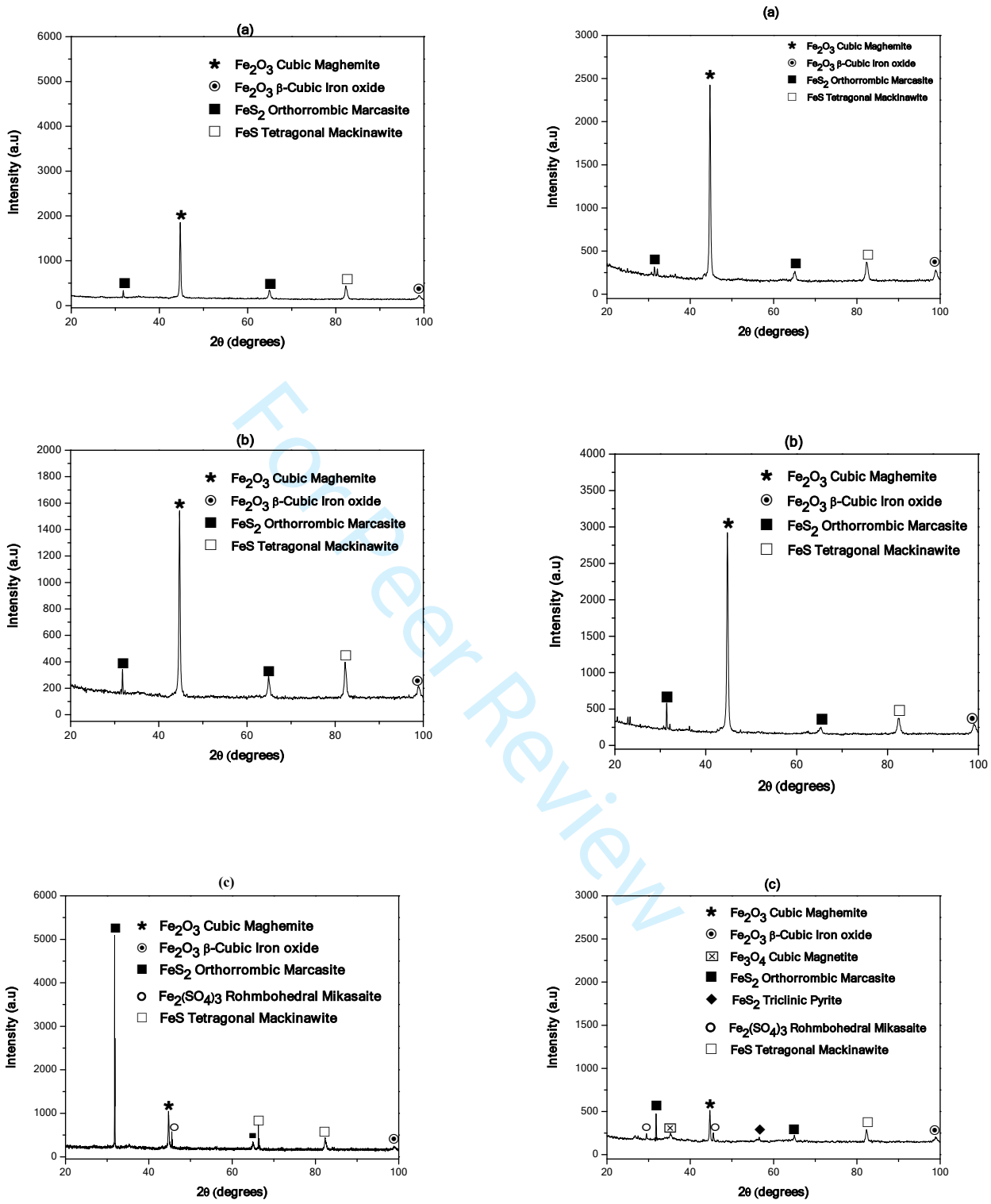

Fig. 15 XRD patterns of the corrosion products formed on steel surface in naturally aerated sour brine with 200 ppm of CI at (a) 30 °, (b) 60 ° and (c) 90 ° at 1.1 m/s (left) and 2.4 m/s (right).

Fig. 14 shows the diffraction patterns obtained for the steel coupons at a flow rate of 1.1 m/s and 2.4 m/s for the angles indicated without inhibitor in naturally aerated sour brine. At 1.1 m/s and 30°, the formation of marcasite (FeS_2) is favored (56,000 a.u). At 60 °, marcasite predominated together with the presence of maghemite (Fe_2O_3) and mikasaite ($Fe_2(SO_4)_3$). At 90 °, the presence of sulfides such as FeS_2 tends to be higher than the other phases though mikasaite and maghemite became evident. At 2.4 m/s, oxides in the form of maghemite predominated at the experimental angles of 30 °, 60 ° and 90 °; however, sulfides such as mackinawite and marcasite are also present though in apparent minor contents. When corrosion inhibitor is added (Fig. 15) at 1.1 m/s, oxides predominated (30 °, 60 °) along with the presence of sulfides, then sulfides (90 °) became prevalent. At. 2.4 m/s, oxides predominated again with minor contents of sulfides (30 °, 60 °) and then a mixture of oxides and sulfides coexist (90 °). The presence of marcasite (FeS_2) as a metastable corrosion product in lieu of cubic pyrite [47] might contribute to corrosion mitigation, because of the adherence of the cubic crystal lattice on the steel surface [48, 49]. The effect of CI is observed in a considerable reduction of peak heights and number of the different corrosion products and some of them became traces after its addition. At 2.4 m/s, the effect of oxygen contamination (~3.4 ppm) is observed more clearly as oxides predominated over sulfides; whereas at 1.1 m/s sulfides prevailed for the angles under testing. Mackinawite was present as a precursor of other corrosion products and appeared on steel for the three impingement angles in static and dynamic conditions (1.1 m/s, 2.4 m/s) with CI in relatively low countings (< 500 a.u.) and without CI in high countings (~6,000 a.u.). These conditions were observed experimentally under the action of both flow rates with and without inhibitor. Corrosion inhibitor seems to mitigate oxide formation and support sulfide formation to balance both groups as corrosion products under oxidant conditions.

According to Pourbaix diagram (Fig. 16) at a pH ~4 at an open circuit potential in aqueous sour brine of - 680 mV (SCE), -436 mV (SHE), the chemical species more likely to appear as corrosion products are marcasite (FeS_2). Likewise, adsorbed oxygen and oxidizing conditions convey chemical species into a pseudo passivation by the formation Fe_2O_3 and possibly γ-Fe_2O_3 (marcasite) [50], which agree with the XRD analysis. The effect of CI is observed in a considerable reduction of peak heights and number of the different corrosion products and some of them became traces after its addition. At 2.4 m/s, the effect of oxygen contamination (~3.4

ppm) is observed more clearly as oxides predominated over sulfides; whereas at 1.1 m/s sulfides prevailed for the angles under testing. These conditions were observed experimentally under the action of both flow rates with and without inhibitor. Corrosion inhibitor seems to mitigate oxide formation and support sulfide formation to balance both groups as corrosion products under oxidant conditions.

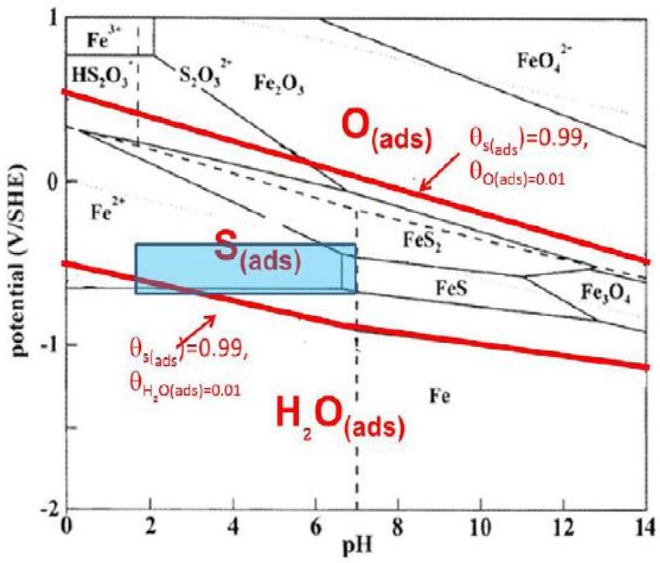

Fig. 16. E-pH diagram for sulfur adsorbed on iron at 25 °C for a total sulfur concentration of 10^{-4} mol/kg. [50]

B. Craig [51] determined an alternative path for oxides when oxygen is present in sour brines suggesting that oxides formation on steel surface as corrosion products are generated as follows.

$$2\,FeS + H_2O + \frac{3}{2}O_2 \rightleftarrows 2\,FeO(OH) + 2S^0$$

The nature of iron sulfides on steel in a wet H_2S environment in the presence of varying oxygen concentrations generated mackinawite consistently. Further oxidation led to FeO(OH) and elemental sulfur, and finally magnetite (Fe_3O_4) when oxidizing conditions prevailed. However, according to current information related to the corrosion mechanism of steel in H_2S [52], marcasite (FeS_2) is not likely to be conformed as a corrosion product in static/dynamic conditions, probably because the experimental work was performed in de-aerated conditions. Further investigation is under way to corroborate the presence/absence of orthorhombic marcasite in aerated/deaerated sour brines. Oxidizing conditions also involves changes in the chemical species formed as corrosion products that became less adherent so carbon steel became

susceptible also to pitting corrosion [44]. The presence of elemental sulfur and adsorbed oxygen to positive electrode potential due to the formation of corrosion products with cations of the type $S_2O_3^{-2}$ might be conformed into mikasaite $(Fe_2SO4)_3$, according to a sequence of the type [50, 53]: tetragonal mackinawite (FeS_{1-x}) → orthorhombic marcasite (FeS_2) → rhombohedral mikasaite $Fe_2(SO_4)_3$ → cubic maghemite (Fe_2O_3) → and orthorhombic magnetite (Fe_3O_4) [54], which is thermodynamically favored [49] instead of either pyrrhotite ($Fe_{1-x}S$) or pyrite (FeS_2) that appeared at relatively high temperature/high H_2S partial pressure [55, 56].

Conclusions

- The presence of sulfides as corrosion products predominated under static and low flow rate over oxides. In contrast, at 2.4 m/s, oxide formation prevailed and led to higher corrosion rates. This might suggest that the oxide film formed in the sour brine contaminated with oxygen might be less protective than the corresponding one conformed of sulfides. Mackinawite is formed in static and dynamic conditions in the absence/presence of corrosion inhibitor and it behaved as a precursor of sulfides/oxides with/without inhibitor. CI seems to balance the formation of sulfides and oxides in aerated conditions.

- Microstructural examination showed that ferrite phase contained in laminar perlite was mainly dissolved with/without inhibitor so cementite behaved as a cathode in the sour brine system. The distribution, morphology and growth of corrosion products/films was conformed in patches and porosity was randomly distributed on surface.

- The highest corrosion rates were determined at 90 ° in dynamic conditions where the estimated normal stresses were apparently higher than the shear stresses. However, the contributing effect of oxygen on corrosion rate remained to be determined.

Acknowledgements

The authors would like to thank the Instituto Politécnico Nacional and the Instituto Mexicano del Petróleo for the facilities provided to perform this work. Conacyt-Mexico is also acknowledged for providing partial financial support to authors.

References

[1] J. Ning, Y. Zheng, D. Young, B. Brown, and S. Nesic, A Thermodynamic model for the prediction of mild steel corrosion products in an aqueous hydrogen sulfide environment, *Corrosion* 2015, **71**, 155-168.

[2] G. Schmitt, W. Bucken, and R. Fanebust, Modelling microturbulences at surface imperfections as related to flow induced localized corrosion. *Corrosion* 1992, **48**, 431-440.

[3] J. Wang and S.A. Shirazi, A CFD based correlation for mass transfer coefficient in elbows, *Int. J Heat Mass Transf. **44*** (2001) 1817-1822.

[4] K.D. Efird, Jet impingement testing for accelerated corrosion, *NACE International Corrosion/2000*, paper no. ***00052***, Houston, TX, US.

[5] Z.D. Cui, S.L. Wu, S.L. Zhu, X.J. Yang, Study on corrosion properties of pipelines in simulated produced water saturated with supercritical CO_2, *J. Appl. Surf. Sci.* 2006*, **252***, 2368-2374.

[6] M. Tjelta and J. Kvarekvål, Electrochemistry of iron sulfide and its galvanic coupling to carbon steel in sour aqueous solutions, *NACE International Corrosion/2016*, paper no. ***07478***, Houston, TX, US.

[7] S. N. Esmaeely, and S. Nesic, Reduction reaction on iron sulfides in aqueous acidic solutions, *J. Electrochem. Soc.* 2017, **164**, C664-C670.

[8] P.P. Bai, H. Zhao, S. Zheng, and C. Chen, Initiation and developmental stages of steel corrosion in wet H_2S environments, *Corros. Sci.* 2015, **52**, 109-119.

[9] Y. Xiong, B. Brown, B. Kinsella, S. Nesic, and A. Pailleret, AFM studies of the adhesion properties of surfactant corrosion inhibitor films, *NACE International Corrosion/2013*, paper no. ***2521***, Houston, TX, US.

[10] G.A. Zhang, and Y.F. Cheng, Electrochemical characterization and computational fluid dynamics simulation of flow-accelerated corrosion of X65 steel in a CO_2-saturated oilfield formation water, *Corros. Sci.* 2010, **52**, 2716-2724.

[11] M. Stern, and A.L. Geary, Electrochemical polarization: I. A theoretical analysis of the shape of polarization curves, *J. Electrochem. Soc.* 1957, **104**, 56-63.

[12] Y.S. Choi, S. Nesic, and S. Ling, Effect of H_2S on the CO_2 corrosion of carbon steel in acidic solutions, *Electrochim. Acta,* 2011, **56**, 1752-1760.

[13] S. Gómez González, Solidworks office profesional. Ed. Marcombo, España 2007.

[14] Ansys Fluent 12, theory guide, April 2009.

[15] W.P. Jones, and B.E. Launder, The Prediction of laminarization with a two-equation model of turbulence, *Int. J. Heat and Mass Transfer,* 1972, **15**, 301-314.

[16] D.B. Spalding, A novel finite difference formulation for differential expressions involving both first and second derivatives. *Int. J. Num. Math. Eng*., 1972, **4**, 551-559.

[17] G.A. Zhang, Y. Zeng, X.P. Guo, F. Jiang, D.Y. Shi, and Z.Y. Chen, Electrochemical corrosion behavior of carbon steel under dynamic high pressure H_2S/CO_2 environment, *Corros. Sci.* 2012, **65**, 37-47.

[18] F. Cai, W. Liu, X. Fan, M. Lu, J. Zhang, and Q. Du, Electrochemical corrosion behavior of X70 pipeline steel in wall jet zone under jet impingement at high temperature and high pressure CO_2, *NACE International Corrosion/2012*, paper no. **0001270**, Houston, TX. US.

[19] A.K. Shukla, and A. Dewan, Flow and thermal characteristics of jet impingement: Comprehensive review, *Int. J. Heat Tech*. 2017, **35**, 153-166.

[20] W. Rohlfs, J. Jorg, C. Ehrenpreis, M. Rietz, H. Haustein, and R. Kneer, Flow structures and heat transfer in submerged laminar jet impingement, *Proceedings of the 1st Thermal and fluids Engineering Summer Conference, TFESC-1, 2015, New York City, US.*

[21] H. Fujimoto, Y. Suzuki, T. Hama, and H. Takuda, Flow characteristics of circular liquid jet impinging on a moving surface covered with a water film, *ISIJ Int.* 2011, **51**, 1497-1505.

[22] D-J Peng, S Vahedi, and T. Wood, CFD wall shear stress benchmark in stratified to annular transitional flow regimen. Flow Assurance, INTECSEA (UK) Ltd. UK BHR Group, 2013, 229-254.

[23] M.E. Ewing, J.J. Weinandy, and R.N. Christense, Observations of two-phase flow patterns in horizontal tube, *Ind. Eng. Chem. Fund.* 1999, **14**, 337-347.

[24] S. Nesic, Using computational fluid dynamics in combating erosion-corrosion, *Chem. Eng. Sci.* 2006, **61**, 4086-4097.

[25] F. Giralt, and D. Trass, Mass transfer from crystalline surfaces in a turbulent impinging jet, Part I: Transfer by erosion, *Can. J. Chem. Eng.* 1975, **53**, 505-511.

[26] F. Giralt, and D. Trass, Mass transfer from crystalline surfaces in a turbulent impinging jet. Part 2: Erosion and diffusional transfer, *Can. J. Chem. Eng.* 1976, **53**, 148-155.

[27] K.D. Efird, E.J. Wright, J.A. Boros, and T.G. Hailey, Correlation of steel corrosion in pipe flow with jet impingement and rotating cylinder tests, *Corrosion* 1993, **49**, 992-1003.

[28] G.A. Zhang, and Y.F. Cheng, Electrochemical characterization and computational fluid dynamics simulation of flow-accelerated corrosion of X65 steel in a CO_2-saturated oilfield formation water, *Corros. Sci.* 2010, **52,** 2716-2724.

[29] Y. Guo, and D.H. Wood, Measurement in the vicinity of a stagnation point. *Exp. Therm. Fluid. Sci.* 2012, **25:8**, 605-614.

[30] E.A.M Hussein, and M.J. Robinson, Erosion-corrosion of 2205 duplex stainless steel in flowing seawater containing sand particles, *Corros. Sci.* 2007, **49**, 1737-1754.

[31] H.Q. Becerra, C. Retamoso, and D.D. Macdonald, The corrosion of carbon steel in oil-in-water emulsions under controlled hydrodynamic conditions, *Corros. Sci.* 2000, **42**, 561-575.

[32] D. J. Phares, G.T. Smedley, and R.C. Flanagan, The wall shear stress produced by normal impingement of a jet on a flat surface, *J. Fluid Mech.* 2000, **418**, 351-375.

[33] J.L. Dawson, T.H. Shih, D.G. John, and D.A. Eden, Electrochemical testing of differential flow induced corrosion using jet impingement rigs. *NACE International Corrosion/87*, paper no. **453**, Houston, TX, US.

[34] C.V. Tu, J.D. Hooper, and D.H. Wood, Wall pressure and shear stress measurements for normal jet impingement, *11th Australasian Fluid Mechanics Conference, University of Tasmania, 14-18 December 1992.*

[35] K.D. Efird, Jet impingement testing in flow accelerated corrosion. *NACE International Corrosion/2000*, paper no. **52**, Houston, TX, US.

[36] B. Montagné, K. Sodjavi, P. Braganca. A. Meslem, and M. Krisiawan, Experimental investigation of nozzle shape effect on wall shear stress beneath impinging round jet. *Proc. International Conference on Mechanics: Fluid Mechanics, Heat and Mass Transfer*. 2014.

[37] W.P. Jepson, S. Bhongale, and M. Gopal, Predictive model for sweet corrosion in horizontal multiphase slug flow, *NACE International Corrosion/1996*, paper no. **19**, Houston, TX. US.

[38] J.L. Dawson, and C.C. Shih, Corrosion under flowing conditions-an overview and model. *NACE International Corrosion/90*, paper no. **09021**, Houston, TX. US.

[39] M. Bartos, and J.D. Watson, Oilfield corrosion inhibitors under extremely high shear stress conditions, *NACE International Corrosion/2000*, paper no. **00068**, Houston, TX. US.

[40] H. Wang, T. Hong, J. Y. Cai, and W. P. Jepson, Enhanced mass transfer and wall shear stress in multiphase slug flow, *NACE International Corrosion/2002*, paper **02501**, Houston, TX. US.

[41] M. Swidzinski, J. Watson, K. Mackin, and W.P. Jepson, Selection and optimization of corrosion inhibitor treatment for a new multiphase pipeline operating under potentially corrosive conditions, *NACE International Corrosion/2003*, paper no. **03335**, Houston, TX. US.

[42] H.H. Huang, W.T. Tsai, and J.T. Lee, Electrochemical behavior of the simulated heat affected zone of A516 carbon steel in H_2S solution. *Electrochim. Acta* 1996, **41**, 1191-1199.

[43] J.H. Kim, I.S. Kim, and Y.G. Zhang, Flow-accelerated corrosion behavior of SA106 Gr. C weldment. *Mat. Corros.* 2003, **54**, 23-31.

[44] J. Ning, Y. Zheng, B. Brown, D. Young, and S. Nesic, The role of iron sulfide polymorphism in localized H_2S corrosion of mild steel, *Corrosion* 2017, **73**, 155-168.

[45] Y. Zheng, J. Ning, B. Brown, D. Young, and S. Nesic, Mechanistic study of the effect of iron sulfide layers on hydrogen sulfide corrosion of carbon steel. *NACE International Corrosion/2015*, paper no. **5933**, Houston, TX. US.

[46] L. Khaksar, G. Whelan, and J. Shirokoff, Electrochemical and microstructural analysis of FeS films from acidic chemical bath at varying temperatures, pH, and immersion time. *Int J. Corrosion* 2016, article ID **1025261**.

[47] S.N. Smith, Current understanding of corrosion mechanisms due to H_2S in and gas production environments, *NACE International Corrosion 2015*, paper no. **5485**, Houston, TX. US.

[48] D. Ricard, and G. Luther III, Chemistry of iron sulfides, *Chem. Rev.* 2007, **107**, 514-562.

[49] G. Schmitt, Unexpected effect of small oxygen concentrations in sales gas on element currents between pipeline steel and magnetite from black powder, *NACE International Corrosion/2015*, paper no. **5587**, Houston, TX. US.

[50] P. Marcus, and E. Protopopoff, Potential-pH diagrams for adsorbed species: Application to sulfur adsorbed on iron in water at 25°C and 300°C, *J. Electrochem. Soc.* 1990, **137**, 2709-2712.

[51] B. Craig, The nature of iron sulfides formed on steel in an H_2 S-O_2 environment, *Corrosion* 1979, **25**, 136-138.

[52] J. Ning, The role of iron sulfide polymorphism in localized corrosion of mild steel, 2016. *Ph.D. thesis, Ohio University*, pp. 79.

[53] F. Shi, L. Zhang, J. Yang, M. Lu, J. Ding, and H. Li, Polymorphous FeS corrosion products of pipeline steel under highly sour conditions, *Corros. Sci.* 2016, **102**, 103-113.

[54] B. Craig, Corrosion product analysis-A road map to corrosion in oil and gas production. *Mater. Perform*. 2002, **8**, 56-59.

[55] X. Zhong, Y. Wang, J. Liang, L. Chen and X. Song, The coupling effect of O_2 and H_2S on the corrosion of G20 steel in a simulating environment of flue gas injection in the Xinjiang oil field, *Materials* 2018, **11**, 1635; doi:10.3390/ma11091635.

[56] B.W.A. Sherar, P.G. Keech, and D.W. Shoesmith, The effect of sulfide on the aerobic corrosion of carbon steel in near-neutral pH saline solutions, *Corros. Sci.* 2013, **66**, 256-262.

Table 1. Average highest values of shear stresses, turbulence energy and velocity for the metallic coupon at position 2

Impact angle	**30 °**	**60 °**	**90 °**
Average shear stress at 1.1 m/s, Pa / N/m^2	12.6	7.5	6.7
Average shear stress at 2.4 m/s, Pa / N/m^2	33.0	15.0	8.6
Turbulence energy (J/kg) at 1.1 m/s	0.04	0.08	0.043
Turbulence energy (J/kg) at 2.4 m/s	0.04	0.10	0.14
Velocity vector at 1.1 m/s	1.05	0.81	0.5
Velocity vector at 2.4 m/s	2.38	1.8	1.1

Table 2. Average stresses for monophasic flow at 1.1-2.4 m/s

	Shear stress by CFD Pa / N/m^2			**Theoretical shear stress Pa / N/m^2**		**Normal stress Pa / N/m^2**
Impact angle	30 °	60 °	90 °	Giralt-Trass [25, 26]	Effird (90 °) [27]	Phares [32]
Average shear stress at 1.1 m/s	12	7.5	6.7	5.3	6.2	620
Average shear stress at 2.4 m/s	33	15	8.6	21.7	10.1	2880

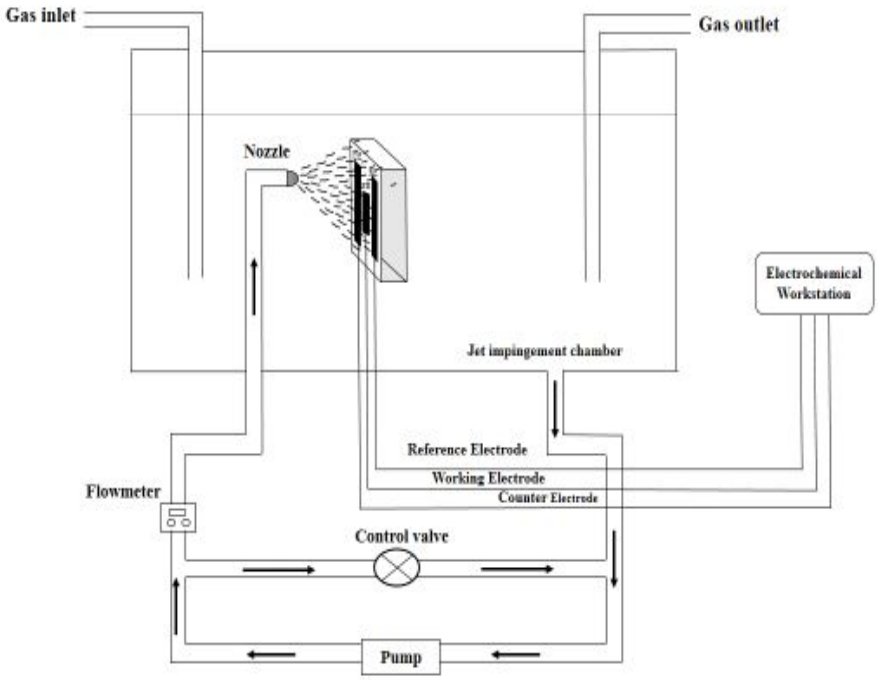

Fig. 1 Schematic diagram of the experimental setup to test flow assisted corrosion (FAC).

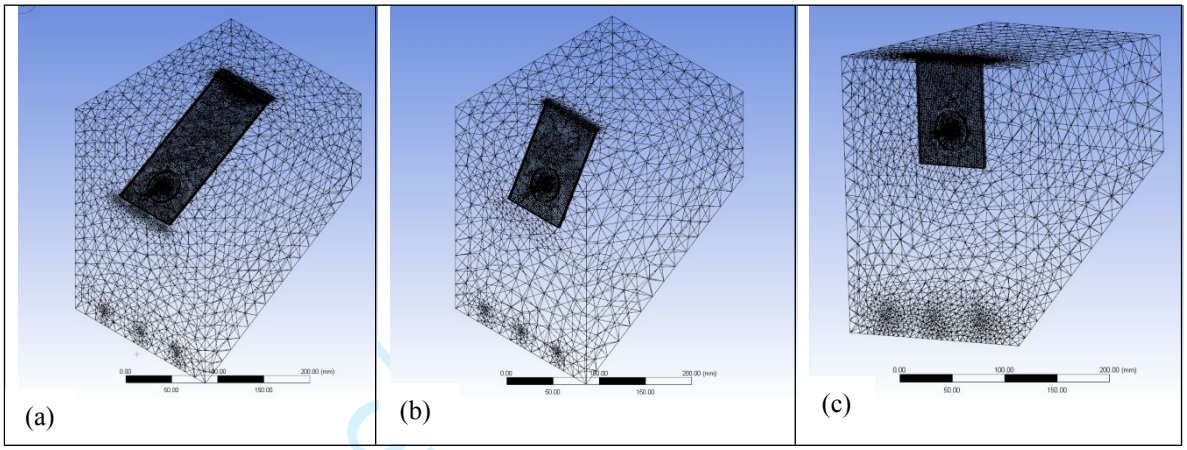

Fig. 2 Scheme of the network generated for the JI chamber showing the plate for the impact angles of (a) 30 °C, (b) 60 °C and (c) 90 °C.

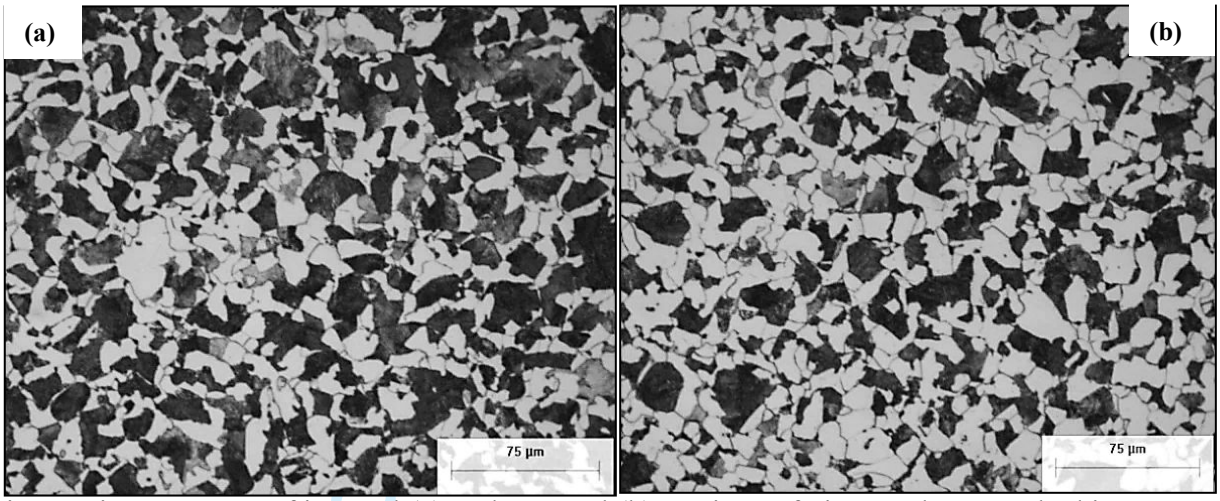

Fig. 3 Microstructure of internal (a) and external (b) sections of pipe steel X70 etched in 5% Nital, showing ferrite and pearlite in light and dark contrast, respectively (500X).

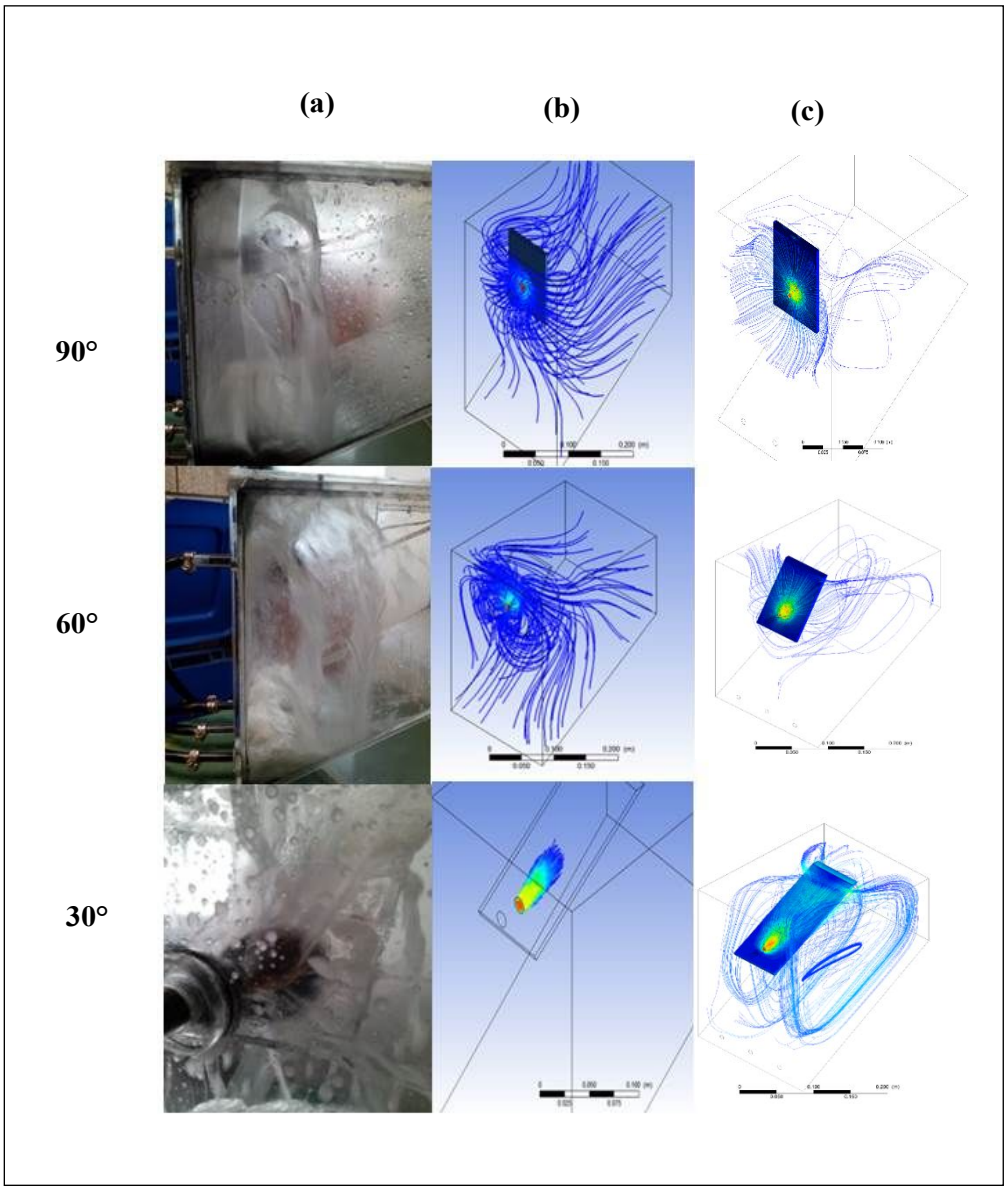

Fig. 4 CFD simulation in the JI chamber showing: (a) Inner flow turbulence produced by impinging on holding plates at the angles indicated; (b) flow density and (c) flow lines at 2.4 m/s.

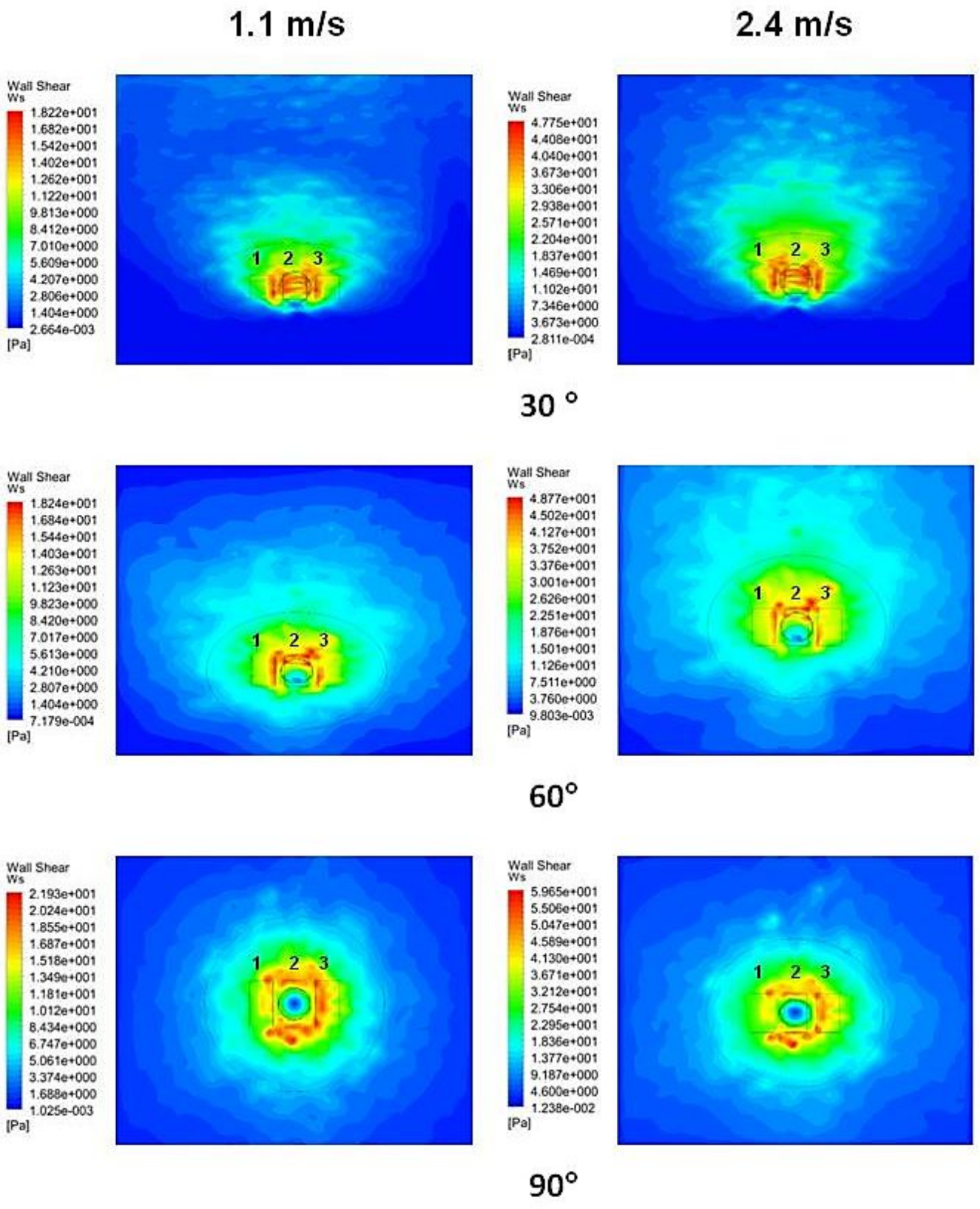

Fig. 5 Distribution of shear stress on steel coupons of X70 under the action of flow rate and impact angles.

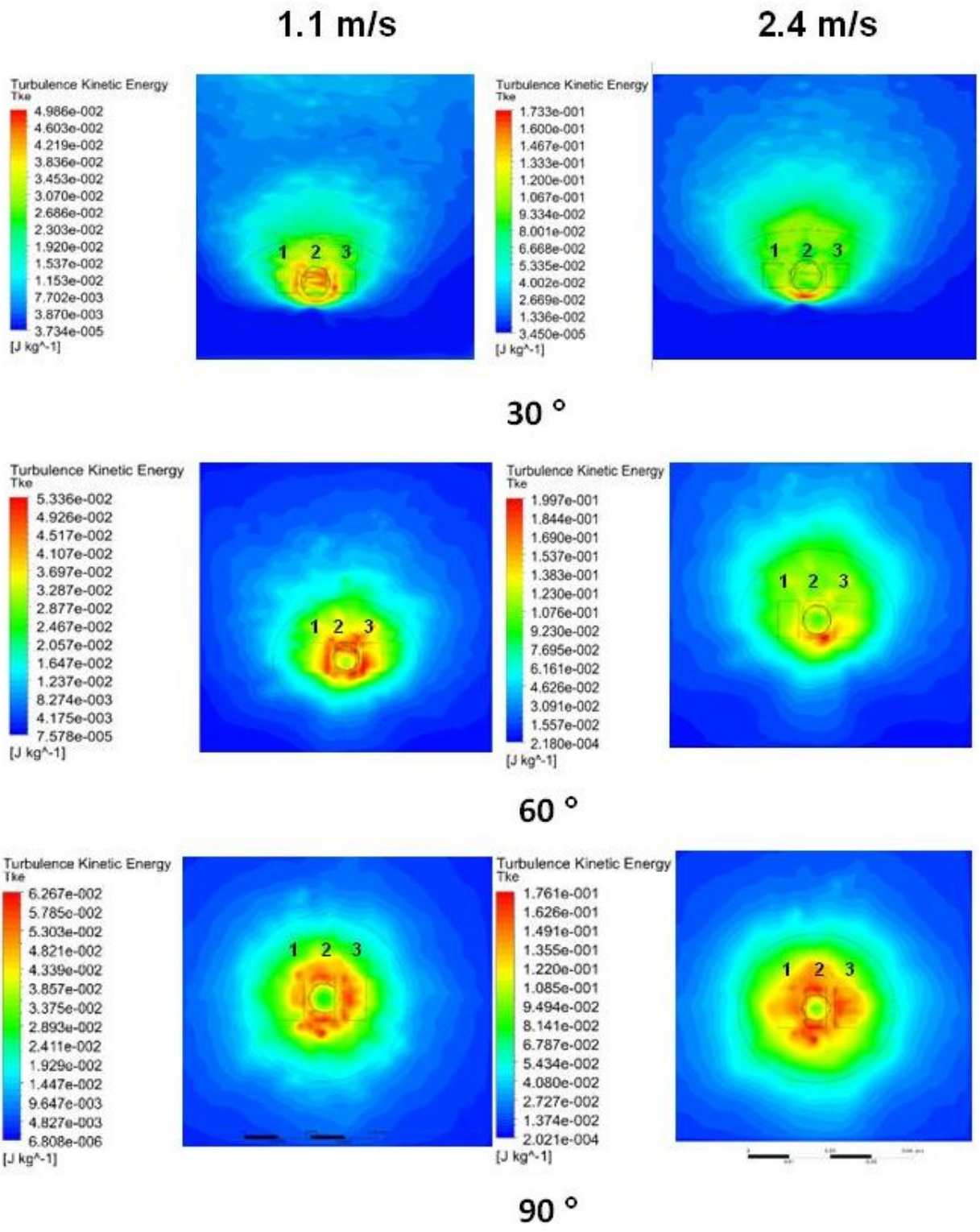

Fig. 6 Distribution of the kinetic energy of turbulence on steel coupons of X70 at the flow rate and impact angle indicated.

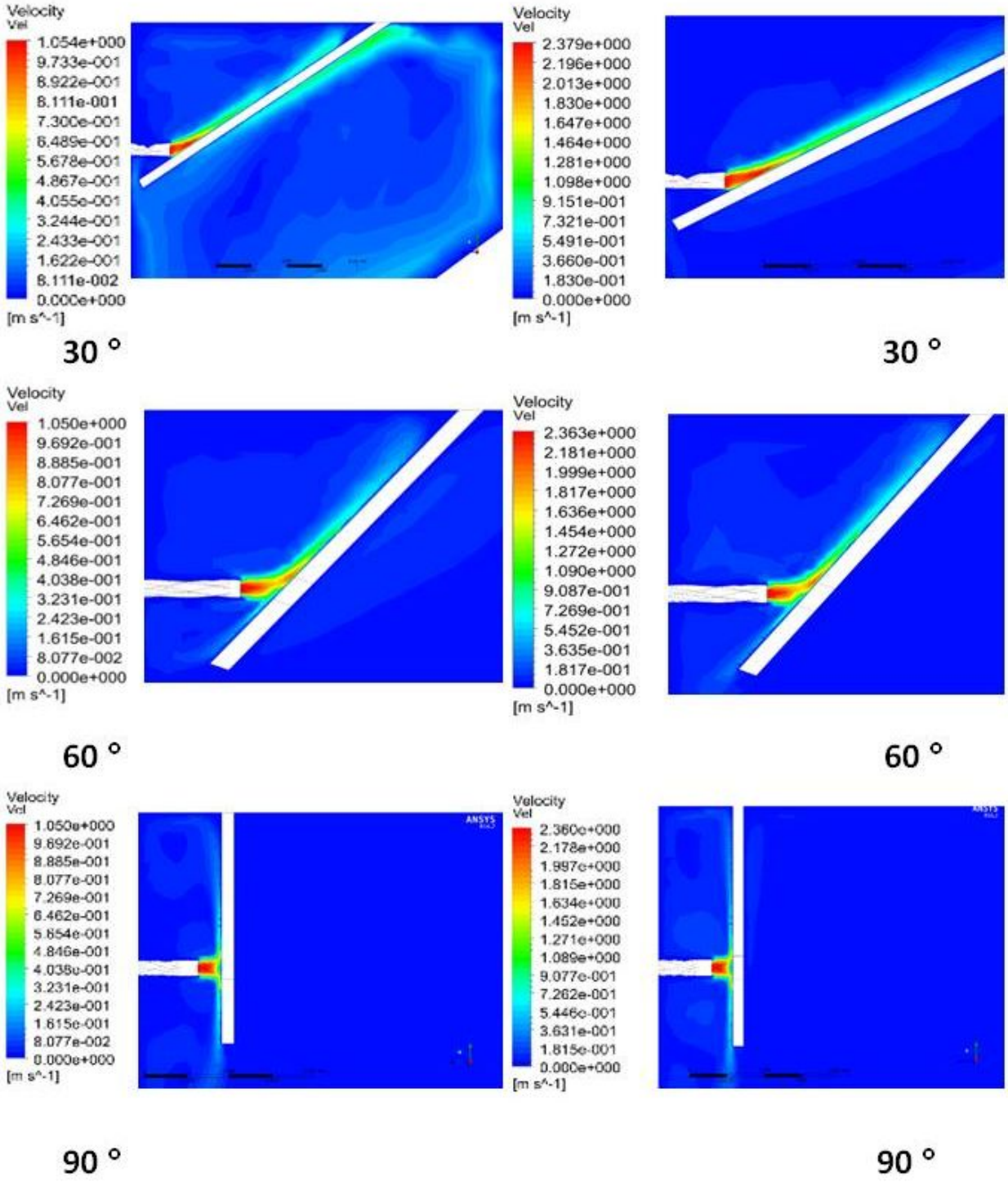

Fig. 7 Distribution of velocity vector on the impingement steel coupons of X70 at the flow rate and impact angle indicated.

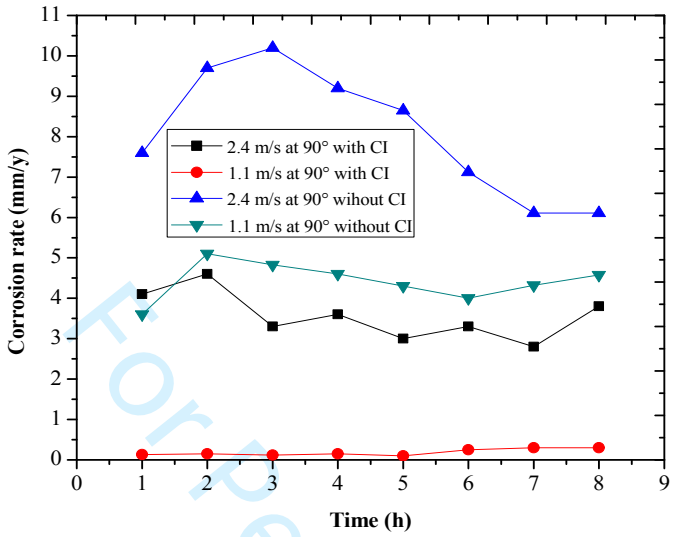

Fig. 8 Corrosion rate at a flow rate of 1.1 m/s and 2.4 m/s (a) without CI, and (b) with CI at an angle of impingement of 90 °.

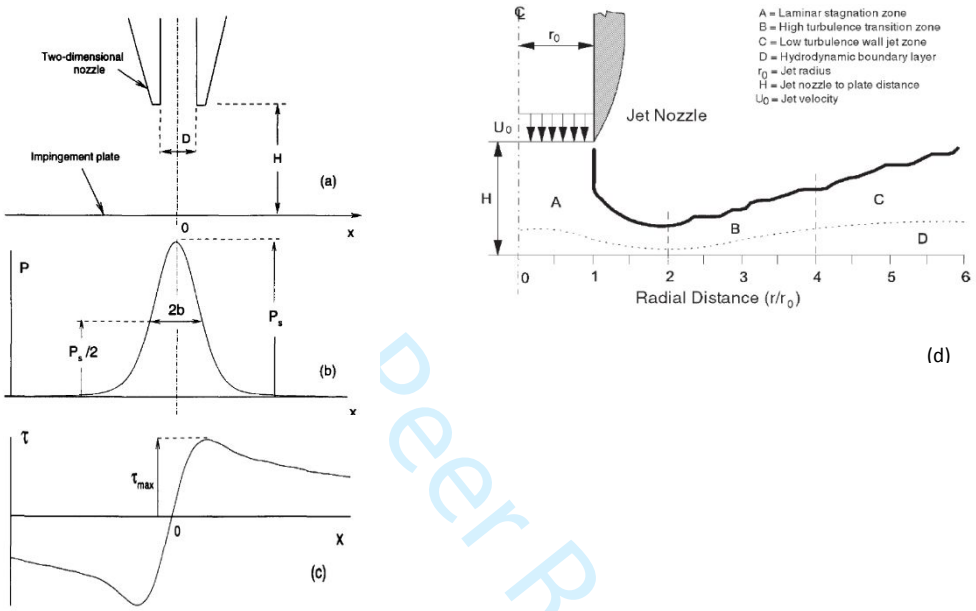

Fig. 9 (a) Jet nozzle and impingement plate (b) Highest normal stress and (c) Highest shear stress under the action of jet impingement on metallic surface in submerged conditions [32], and (d) a schematic diagram of the JI system along with flow patterns after impingement [33]

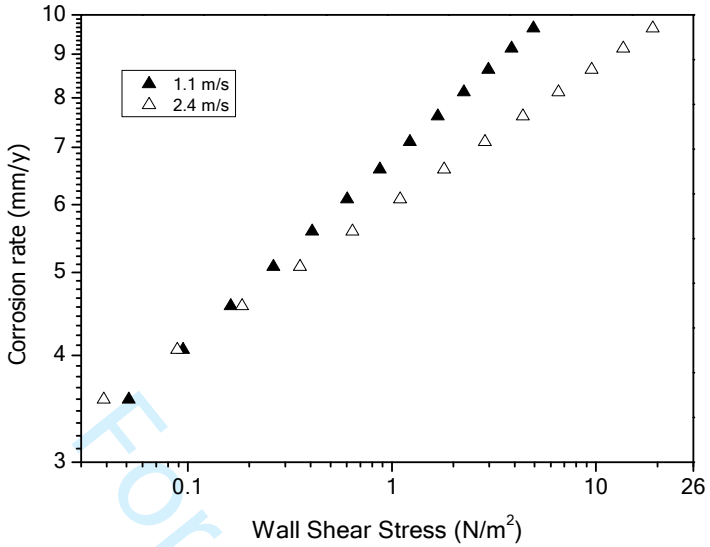

Fig. 10 Wall shear stress determined according to Efird´s equation from the experimental data of corrosion rate obtained in the JI chamber at 90 °.

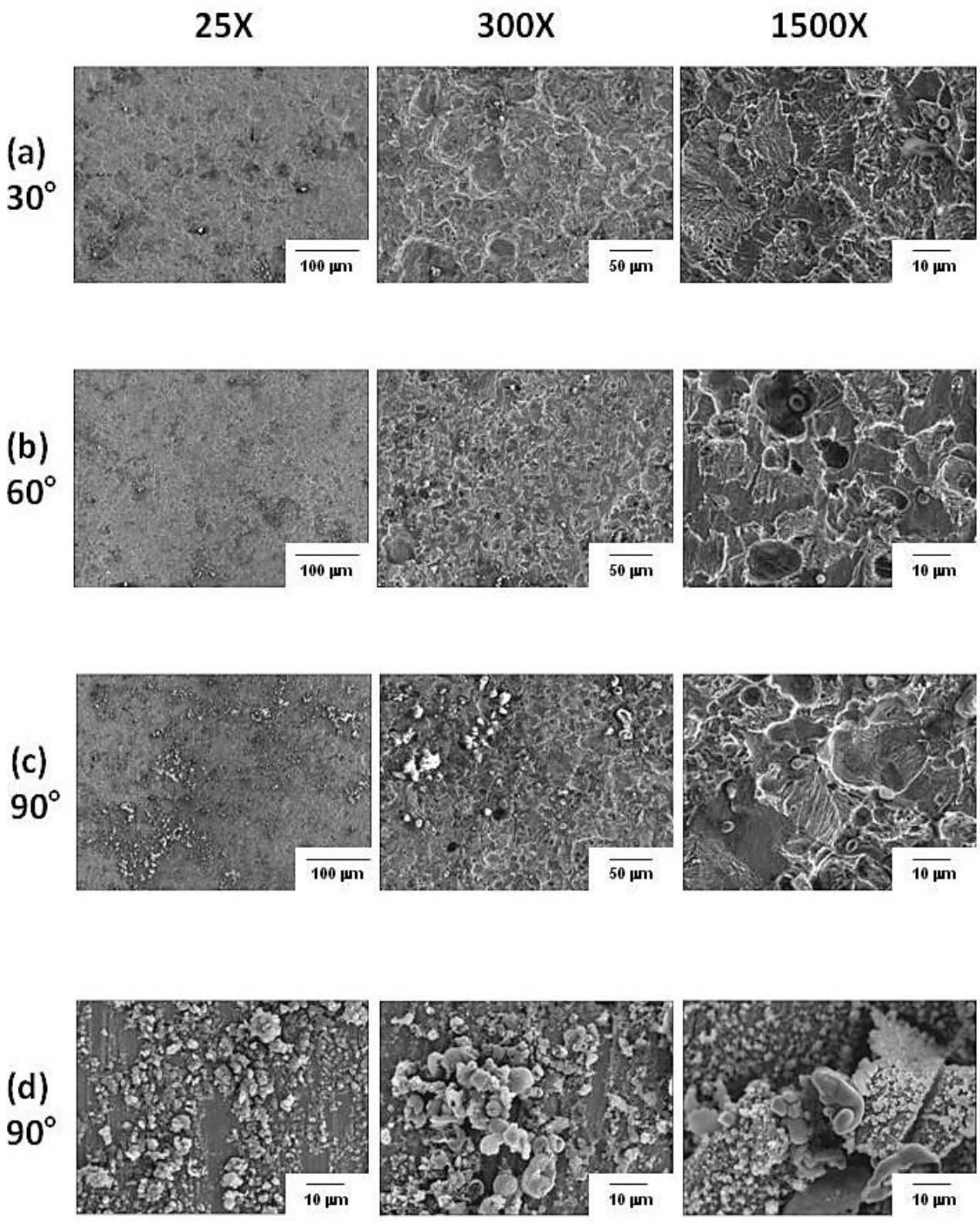

Fig. 11 SEM micrographs of X-70 in naturally aerated sour brine without inhibitor (a-c) and with inhibitor (d) after 8 h at 1.1 m/s

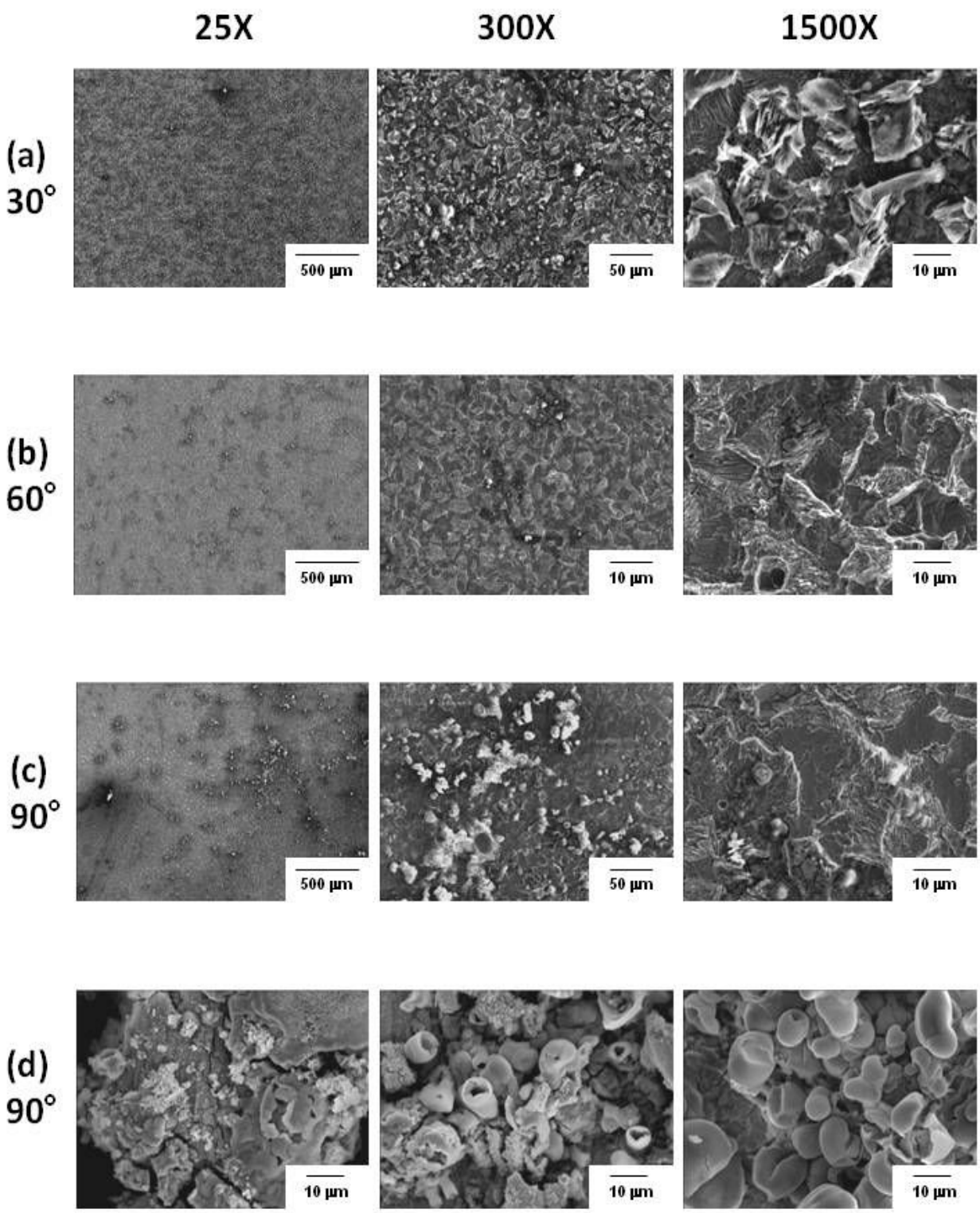

Fig. 12 SEM micrographs of X70 in naturally aerated sour brine without inhibitor (a-c) and with inhibitor (d) after 8 h at 2.4 m/s

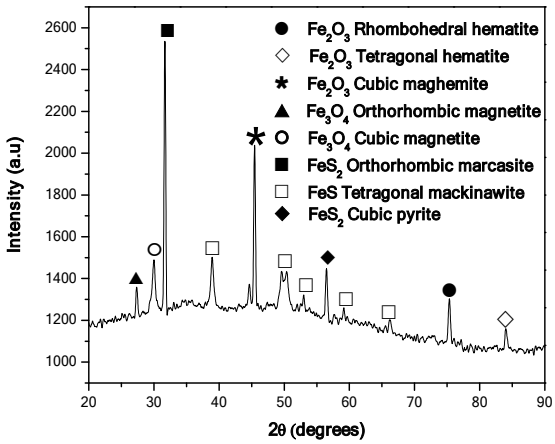

Fig. 13 XRD pattern of the corrosion products formed on steel in static condition after an immersion for 24 hours in naturally aerated sour brine.

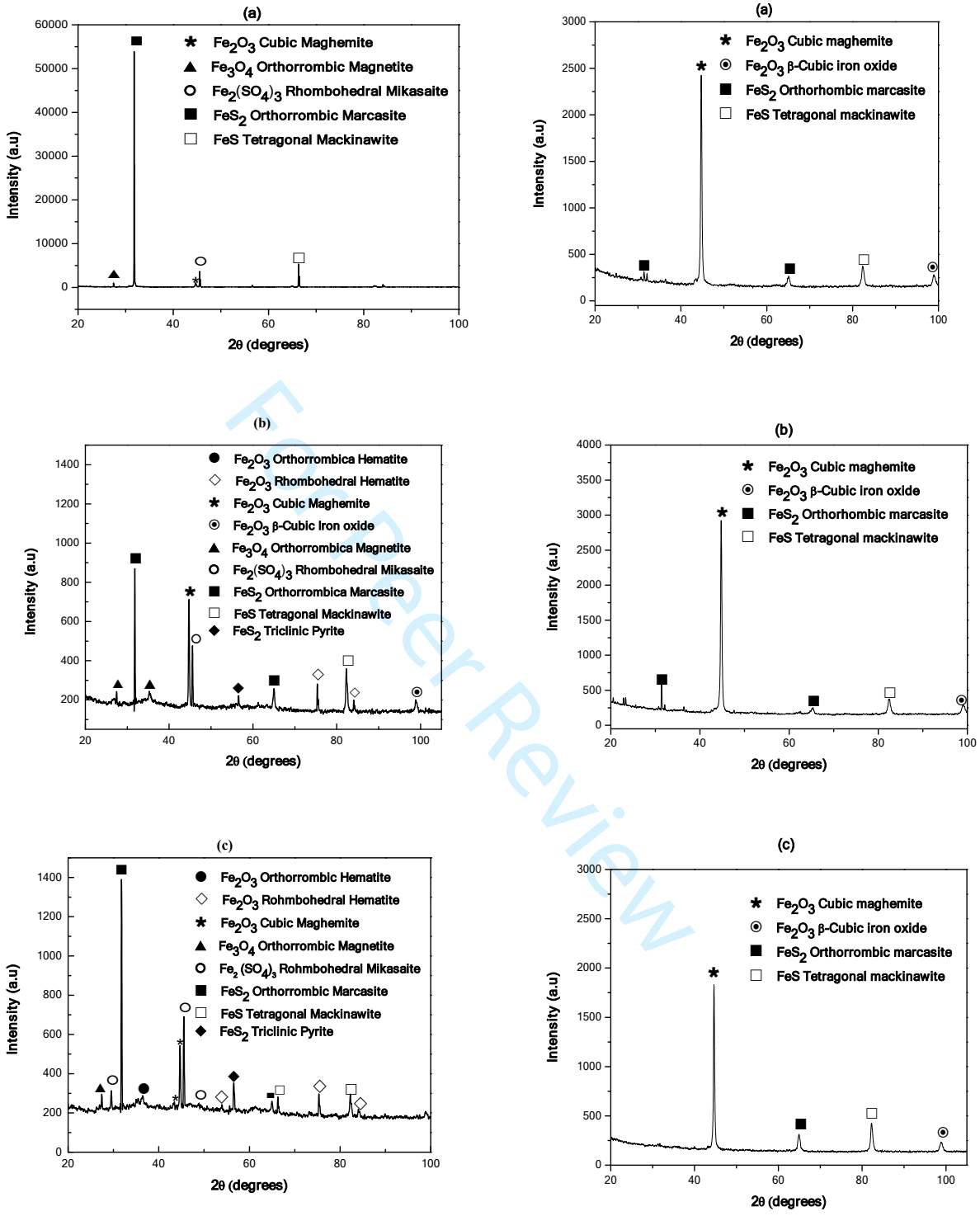

Fig. 14 XRD patterns of the corrosion products formed on steel surface in naturally aerated sour brine without CI (a) 30 °, (b) 60 ° and (c) 90 ° at 1.1 m/s (left) and 2.4 m/s (right).

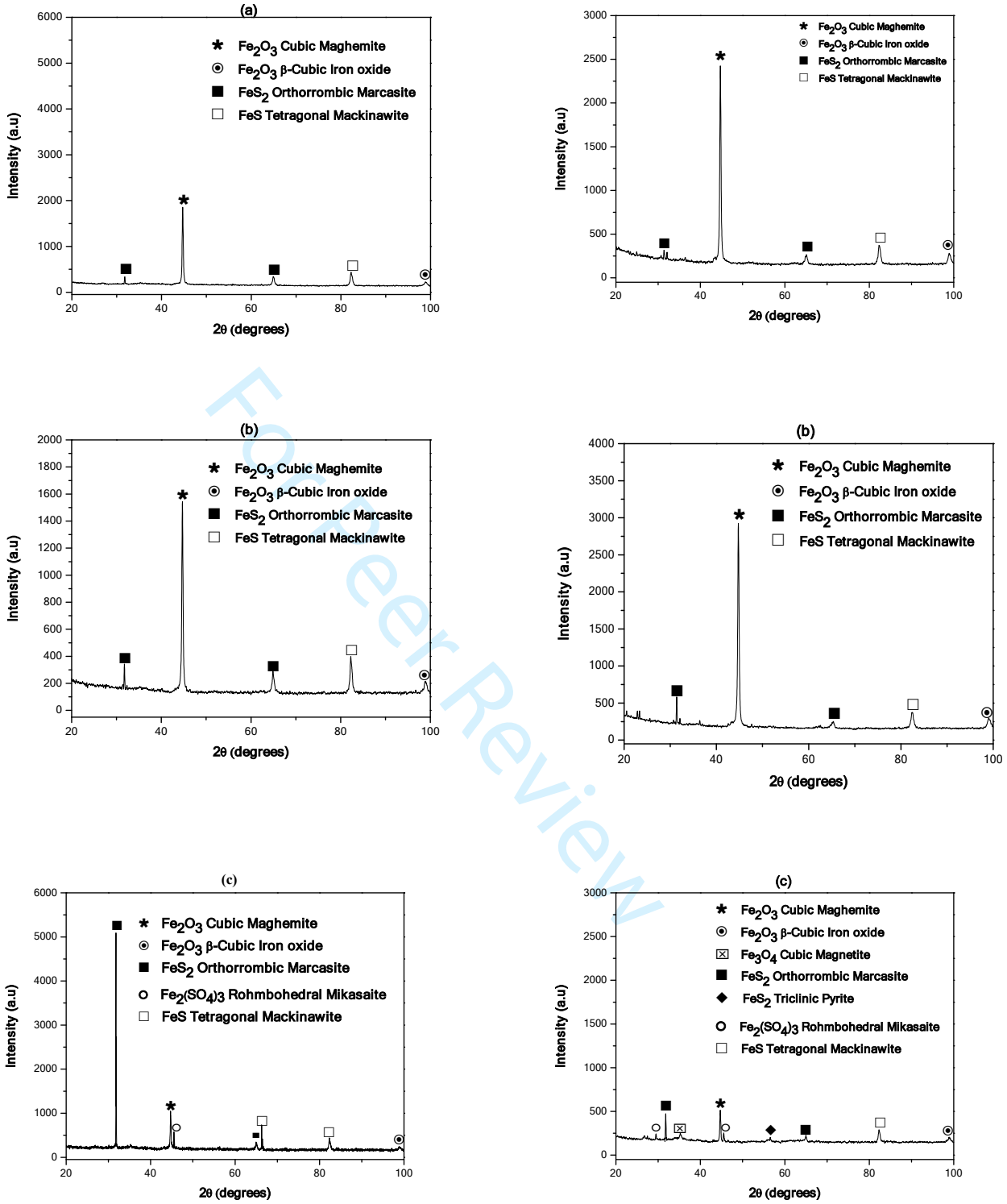

Fig. 15 XRD patterns of the corrosion products formed on steel surface in naturally aerated sour brine with 200 ppm of CI at (a) 30 °, (b) 60 ° and (c) 90 ° at 1.1 m/s (left) and 2.4 m/s (right).

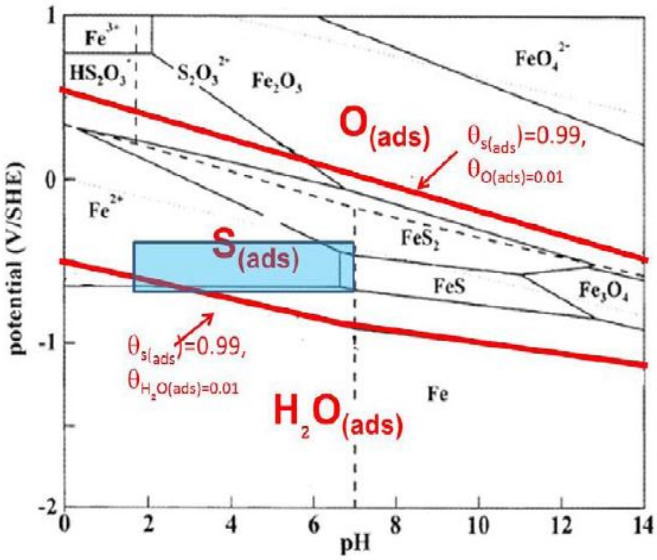

Fig. 16. E-pH diagram for sulfur adsorbed on iron at 25 °C for a total sulfur concentration of 10^{-4} mol/kg. [50].